

FINITE DIFFERENCE ANALYSIS OF PLANAR OPTICAL WAVEGUIDES

M. S. Stern

1. Introduction
 2. Vector Helmholtz Wave Equation
 3. Scalar Modes
 4. Quasi-TE (E_x) Modes
 5. Quasi-TM (E_y) Modes
 6. H_y Modes
 7. H_x Modes
 8. Finite Difference Matrices
 9. Inverse Power Iteration Method
 10. Triangular Factorization of a Matrix
 11. Rayleigh Quotient Solution
 12. Iterative Methods for Linear Algebraic Equations
 13. Numerical Results for Single Rib Waveguides
 14. Numerical Results for Rib Waveguide Directional Couplers
 15. Numerical Results for Embedded Waveguides
 16. Conclusion
- References

1. Introduction

Planar optical waveguides, such as rib, embedded, channel, embossed and buried structures, have various important applications in the field of integrated optics as passive and active devices, typical examples of which include bends, tapers, splitters, routing switches, laser cavities, and modulators. All of the waveguiding structures listed near the beginning of the preceding sentence fall within the scope of those

displayed in Figures 1 and 2 with appropriate choices of geometrical and optical parameters. For example, Figure 2 would represent a channel waveguide when $H = 0$ or a buried waveguide when $n_c = n_s$, whilst both figures would depict an embossed waveguide when $D = 0$. The directions of the axes assumed throughout this chapter are also shown in these figures.

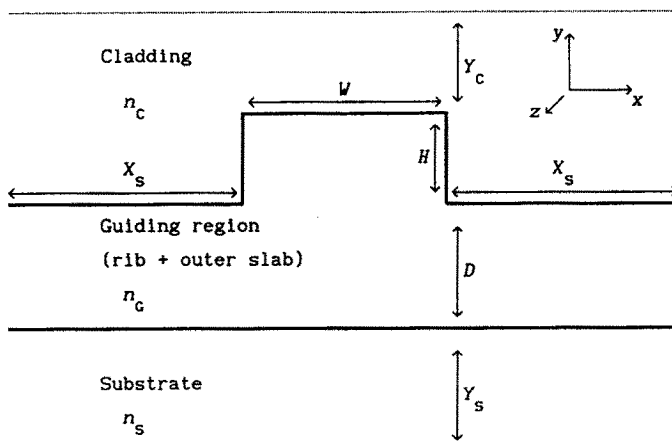


Figure 1. Typical semiconductor rib waveguide structure. The refractive indices of the three regions are n_g , n_s , and n_c . The directions of the axes are also shown. (©IEE [7,8,14] 1988, 1991)

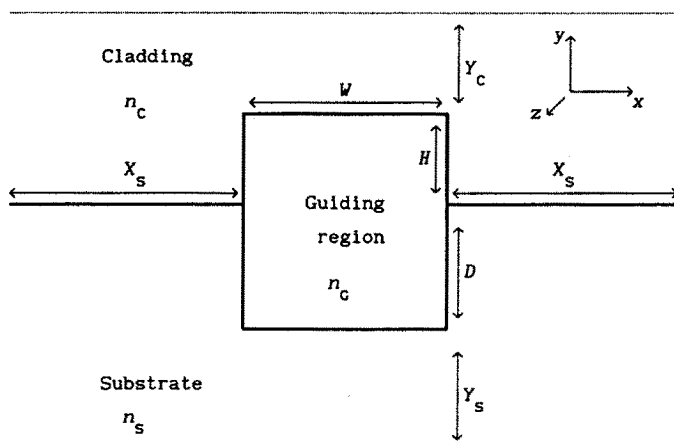


Figure 2. Typical semiconductor embedded waveguide structure. The refractive indices of the three regions are n_g , n_s , and n_c . The directions of the axes are also shown. (©IEE [8,14] 1988,1991)

Since the early 1980s there has been considerable interest and activity in the numerical analysis and modeling of planar waveguide structures because of their important integrated optics applications. A group of powerful techniques, which have been and continue to be employed to analyze and model propagation modes for a very wide range of transverse refractive index profiles $n(x, y)$ in longitudinally invariant dielectric waveguides, are the finite difference methods [1–18]. They are particularly suitable for application to structures with piecewise constant $n(x, y)$ where each internal dielectric interface is parallel to either the xz plane or the yz plane (as in Figures 1 and 2). Moreover, they are also highly effective with (transversely) graded index structures [4,11,12,15]. The nature of the two-dimensional variation of $n(x, y)$, whether piecewise constant or graded, precludes exact analytical solutions of the electromagnetic field problem for planar waveguides unless the latter are purely step-index slab structures consisting of at least three uniform layers ($-\infty \leq x \leq \infty$, $-\infty \leq z \leq \infty$) [16,19–22].

Before employing a finite difference method to determine the modal indices and field profiles of a longitudinally invariant planar optical waveguide it is frequently convenient to represent the latter's transverse index profile $n(x, y)$ by the rectangular cell array structure illustrated in Figure 3, with a grid point located at the center of each cell of constant refractive index and changes in refractive index being permitted only at cell boundaries. This results in each internal dielectric interface being placed halfway between adjacent finite difference grid lines [7,8,14,16]. Alternative rectangular cell array representation of $n(x, y)$, where dielectric discontinuities are not located midway between adjacent grid lines, are also in use [5,6,11–13,15,17]. This chapter will concentrate on finite difference schemes based on cell-centered grid points. It should be noted that finite difference methods based on rectangular cell array representation of $n(x, y)$, whether or not the grid points are cell-centered, can usually model planar waveguide structures, e.g., directional couplers, containing more dielectric interfaces than shown in Figures 1 and 2, as will be demonstrated in later sections of this chapter.

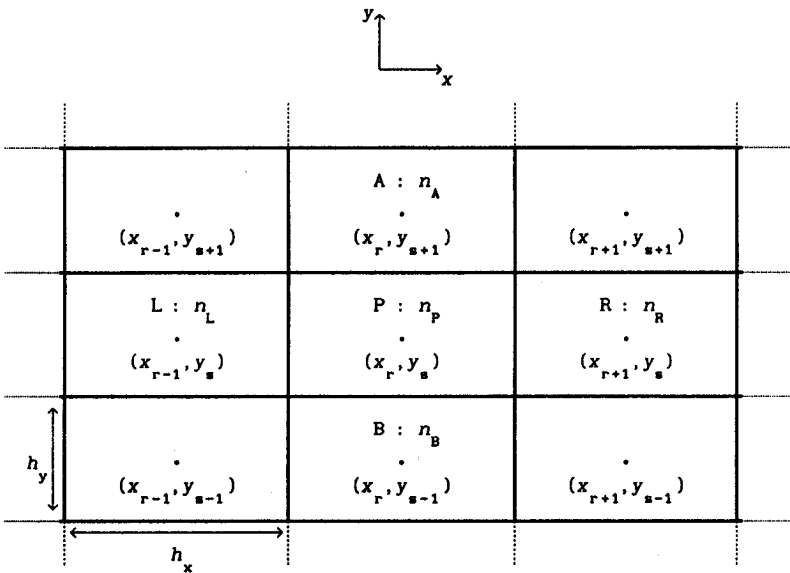


Figure 3. Cell structure of the finite difference grid. The center coordinates and constant refractive index of each cell involved in forming a five-point difference approximation at the point (x_r, y_s) are shown. Changes in refractive index occur only at cell boundaries. Each cell has sides of length h_x and h_y . (©IEE [7,8,14] 1988,1991)

The accuracy of finite difference solutions of optical waveguiding problems depends not only on the grid discretization, i.e., the magnitudes of the horizontal and vertical set lengths h_x and h_y respectively, but also on approximations assumed about the nature of the electromagnetic field within the waveguiding structure. The numerical analysis may be carried out at one of three levels which are listed below in order of increasing mathematical and physical complexity:

(i) For *scalar* modes, the electric and magnetic fields and their gradients are assumed to be completely continuous throughout the modeled waveguide structure [1-4,7,9,13,16,23-26]. Such modes are the eigen-solutions of a single scalar Helmholtz equation which may be replaced at each internal grid point by the usual five-point difference approximation. The latter will be derived in Section 3 for completeness. This mathematical/physical model provides a reasonable approximation for TE modes in dielectric waveguides where there is very little variation of the refractive index profile in the x direction [3,4,7,9,23-26].

(ii) For *semi-vectorial* modes, one of the transverse components of either the electric field \vec{E} or the magnetic field \vec{H} is assumed to be of negligible magnitude, usually zero, compared with the other five components [7–9,14,16–18,26–31]. It is then shown in Sections 4–7 below that the latter five components of the electromagnetic field can be expressed in terms of the non-zero transverse component belonging to the field vector containing the neglected component [7,8,16,26]. This *principal* transverse component satisfies a single scalar Helmholtz equation and is subject to appropriate *continuity* and *discontinuity* conditions at each internal dielectric interface [7,8,14,16,17,26]. The semi-vectorial approach is supported by laboratory experiments with longitudinally invariant planar optical waveguides having transverse piecewise constant refractive index profiles where each dielectric discontinuity is parallel to either the xz or yz plane; it has been observed that such structures preferentially propagate \vec{E} -field polarizations which are parallel to either the xz plane (quasi-TE modes) or the yz plane (quasi-TM modes) and that these polarizations tend to persist unchanged over thousands of wavelengths. Theoretical support for the semi-vectorial concept is provided by a rigorous mathematical analysis presented in the second chapter of reference [26] and by material appearing in [16].

(iii) In full *vectorial* (or vector) investigations of optical waveguiding problems no electromagnetic field component, however small in magnitude it may be throughout the waveguide structure, is neglected. However, calculations are performed only in terms of either the vector E -field [32] or the vector H -field [5,6,12,15,33–42]; the three components of the other field are then available implicitly via Maxwell's equations. If the numerical method employed to solve the vector problem involves all three components of the chosen field, then spurious modes usually arise and they have to be eliminated by use of a penalty function that involves an arbitrary parameter [33–36,38, 39]. However, spurious modes can be avoided by imposing the appropriate zero divergence constraint on the chosen field, with the consequence that the resulting equations in the numerical solution scheme will only involve coupling between the two transverse components of the field [5,6,12,15,40–42]; the axial component is then available implicitly via the zero divergence constraint. This chapter will concentrate on finite difference solutions of scalar and semi-vectorial optical waveguiding problems, particularly the latter. There will also be some consideration of the associated numerical linear algebra in Sections 9, 10 and 12. Readers who are in-

interested in finite difference solutions of vector field problems, without spurious modes, are advised to consult references [5,6,12,15].

2. Vector Helmholtz Wave Equation

For harmonic wave propagation in the positive z direction along a longitudinally invariant planar optical waveguide, we consider the fields (in the usual notation)

$$\overline{E}(x, y, z, t) = (E_x, E_y, E_z) \exp j(\omega t - \beta z) \quad (1a)$$

$$\overline{H}(x, y, z, t) = (H_x, H_y, H_z) \exp j(\omega t - \beta z) \quad (1b)$$

$$\overline{D} = \varepsilon(x, y) \overline{E} \quad , \quad \overline{B} = \mu \overline{H} \quad (2)$$

where the permittivity $\varepsilon(x, y)$ is usually piecewise constant and the permeability μ completely constant throughout the solution domain. The amplitude components of the electric and magnetic fields in (1) are functions only of x and y . (The components of \overline{B} and \overline{D} may be similarly defined). Then, from Maxwell's equations for source-free regions, namely,

$$\nabla \cdot \overline{D} = 0 \quad , \quad \nabla \cdot \overline{B} = 0 \quad (3a)$$

$$\nabla \times \overline{E} = -\frac{\partial \overline{B}}{\partial t} = -j\omega\mu\overline{H} \quad (3b)$$

$$\nabla \times \overline{H} = \frac{\partial \overline{D}}{\partial t} = j\omega\varepsilon\overline{E} \quad (3c)$$

we obtain

$$\nabla \times (\nabla \times \overline{E}) = \nabla(\nabla \cdot \overline{E}) - \nabla^2 \overline{E} = \omega^2 \varepsilon \mu \overline{E} = k^2 \overline{E} \quad (4)$$

in which

$$k(x, y) = \omega(\varepsilon\mu)^{1/2} = 2\pi n(x, y)/\lambda \quad (5)$$

where λ is the free-space wavelength. By taking the divergence of the extreme left and right hand sides of (4) we find that

$$\nabla \cdot \overline{E} = -(1/k^2) \overline{E} \cdot \nabla k^2 = -\overline{E} \cdot \nabla \log_e k^2 \quad (6)$$

which may be substituted into (4) to yield the vector wave equation

$$\nabla^2 \bar{E} + k^2 \bar{E} + \nabla \left(\frac{\bar{E} \cdot \nabla k^2}{k^2} \right) = \nabla^2 \bar{E} + k^2 \bar{E} + \nabla (\bar{E} \cdot \nabla \log_e k^2) = 0 \quad (7)$$

In regions of piecewise constant refractive index, (5) yields

$$\nabla k^2 = 0 = \nabla \log_e k^2 \quad (8)$$

Furthermore, it should be noted that ∇k^2 and $\nabla \log_e k^2$ are undefined wherever $k(x, y)$ is discontinuous [43,44], i.e., at internal dielectric interfaces. Hence, by observing that (1) gives the identities

$$\partial/\partial z \equiv -j\beta \quad , \quad \partial^2/\partial z^2 \equiv -\beta^2 \quad (9)$$

we find that, for longitudinally invariant optical waveguides with transverse piecewise constant refractive index profiles, equation (7) reduces to the vector \bar{E} Helmholtz wave equation

$$\nabla_T^2 \bar{E} + k^2 \bar{E} = \beta^2 \bar{E} \quad (10)$$

in which the transverse Laplacian is

$$\nabla_T^2 = \partial^2/\partial x^2 + \partial^2/\partial y^2 \quad (11)$$

The vector \bar{H} Helmholtz wave equation

$$\nabla_T^2 \bar{H} + k^2 \bar{H} = \beta^2 \bar{H} \quad (12)$$

may be similarly derived for such waveguide structures.

For transverse graded index dielectric waveguides, substitution of the result (9) into (7) leads to

$$\nabla_T^2 \bar{E}_T + (k^2 - \beta^2) \bar{E}_T = -\nabla_T \left(\frac{\bar{E}_T \cdot \nabla_T k^2}{k^2} \right) \quad (13)$$

in which

$$\bar{E}_T(x, y, z, t) \equiv (E_x, E_y, 0) \exp j(\omega t - \beta z) \quad (14)$$

and

$$\nabla_T \equiv \left(\frac{\partial}{\partial x}, \frac{\partial}{\partial y}, 0 \right) \quad (15)$$

The longitudinal component of the \overline{E} -field is then obtained from the zero-divergence constraint in the form

$$E_z = - \left(\frac{j}{\beta k^2} \right) \nabla_T \cdot (k^2 \overline{E}_T) \quad (16)$$

The x component of (13) yields

$$\frac{\partial}{\partial x} \left(\frac{\partial E_x}{\partial x} + \frac{E_x}{k^2} \frac{\partial k^2}{\partial x} \right) + \frac{\partial^2 E_x}{\partial y^2} + (k^2 - \beta^2) E_x = - \frac{\partial}{\partial x} \left(\frac{E_y}{k^2} \frac{\partial k^2}{\partial y} \right)$$

which can be rewritten as

$$\frac{\partial}{\partial x} \left(\frac{1}{k^2} \frac{\partial}{\partial x} (k^2 E_x) \right) + \frac{\partial^2 E_x}{\partial y^2} + (k^2 - \beta^2) E_x = - \frac{\partial}{\partial x} \left(\frac{E_y}{k^2} \frac{\partial k^2}{\partial y} \right) \quad (17)$$

Similarly, the y component of (13) leads to

$$\frac{\partial^2 E_y}{\partial x^2} + \frac{\partial}{\partial y} \left(\frac{1}{k^2} \frac{\partial}{\partial y} (k^2 E_y) \right) + (k^2 - \beta^2) E_y = - \frac{\partial}{\partial y} \left(\frac{E_x}{k^2} \frac{\partial k^2}{\partial x} \right) \quad (18)$$

The coupling between these two equations vanishes when the \overline{E} -field is parallel to either the xz or yz plane. For the former polarization it is only necessary to solve (17) with its right-hand side set to zero, whilst in the case of the latter polarization, equation (18) is considered with its right-hand side equal to zero. Obviously, in regions of piecewise constant refractive index, equations (13), (17), and (18) reduce to the familiar Helmholtz equation (10).

The remainder of this chapter will be mainly concerned with *scalar* and, in particular, *semi-vectorial* solutions of (10) and (12) for waveguide structures with transverse piecewise constant refractive index profiles. This approach is justified by the fact that *no* finite difference grid points will coincide with any dielectric discontinuities (where ∇k^2 is undefined).

3. Scalar Modes

Scalar modes are the eigensolutions of the equation

$$\nabla_T^2 E_z + k^2 E_z = \beta^2 E_z \quad (19)$$

where E_z , $\partial E_z/\partial x$, and $\partial E_z/\partial y$ are continuous throughout the solution domain. The component H_z , which also satisfies (19), and its gradients possess the same continuity properties.

The usual five-point difference approximation for (19) will now be established. With reference to Figure 3, we define the notation

$$k_{r,s} = k(x_r, y_s) \quad , \quad E_{r,s} = E_z(x_r, y_s) \quad , \text{etc}$$

and consider the Taylor series

$$E_{r+1,s} = \sum_{m=0}^{\infty} \left(\frac{h_x^m}{m!} \right) \left(\frac{\partial^m E_z}{\partial x^m} \right)_{r,s} \quad (20a)$$

and

$$E_{r-1,s} = \sum_{m=0}^{\infty} (-1)^m \left(\frac{h_x^m}{m!} \right) \left(\frac{\partial^m E_z}{\partial x^m} \right)_{r,s} \quad (20b)$$

which yield the familiar approximations

$$h_x \left(\frac{\partial E_z}{\partial x} \right)_{r,s} = \frac{E_{r+1,s} - E_{r-1,s}}{2} + O(h_x^3) \quad (21)$$

and

$$h_x^2 \left(\frac{\partial^2 E_z}{\partial x^2} \right)_{r,s} = (E_{r+1,s} - 2E_{r,s} + E_{r-1,s}) + O(h_x^4) \quad (22)$$

A similar analysis leads to the results

$$h_y \left(\frac{\partial E_z}{\partial y} \right)_{r,s} = \frac{E_{r,s+1} - E_{r,s-1}}{2} + O(h_y^3) \quad (23)$$

and

$$h_y^2 \left(\frac{\partial^2 E_z}{\partial y^2} \right)_{r,s} = (E_{r,s+1} - 2E_{r,s} + E_{r,s-1}) + O(h_y^4) \quad (24)$$

The approximations (22) and (24) enable the Helmholtz equation (19) to be replaced by the five-point difference scheme

$$\frac{E_{r,s-1}}{h_y^2} + \frac{E_{r-1,s}}{h_x^2} + (k_{r,s}^2 - 2/h_x^2 - 2/h_y^2) E_{r,s} + \frac{E_{r+1,s}}{h_x^2} + \frac{E_{r,s+1}}{h_y^2} = \beta^2 E_{r,s} \quad (25)$$

at the grid point (x_r, y_s) . By applying this approximation at each internal grid point, with appropriate amendments when (x_r, y_s) is adjacent to the outer boundary of the solution domain, we obtain the algebraic eigenvalue problem

$$A_s \overline{E}_s = \beta_s^2 \overline{E}_s \quad (26)$$

in which A_s is a real *symmetric band* matrix, β_s^2 is the scalar mode propagation eigenvalue, and \overline{E}_s is the corresponding normalized eigenvector representing the field profile $E_z(x, y)$. The solution of (26), and of the corresponding matrix eigenvalue problems generated by the semi-vectorial polarized finite difference (SVFD) schemes derived in Sections 4–7, will be discussed in Section 8.

4. Quasi-TE (E_x) Modes

Quasi-TE modes are defined by the laboratory polarization [7,14,16,17,26]

$$\overline{E}(x, y, z, t) \equiv (E_x, 0, E_z) \exp j(\omega t - \beta z) \quad (27)$$

Then Maxwell's equations (3) yield, in regions of piecewise constant refractive index,

$$E_z = - \left(\frac{j}{\beta} \right) \frac{\partial E_x}{\partial x} \quad (28a)$$

$$H_x = \left(\frac{1}{\omega \mu \beta} \right) \frac{\partial^2 E_x}{\partial x \partial y} \quad (28b)$$

$$H_y = \left(\frac{\beta}{\omega \mu} \right) E_x - \left(\frac{1}{\omega \mu \beta} \right) \frac{\partial^2 E_x}{\partial x^2} \quad (28c)$$

$$H_z = - \left(\frac{j}{\omega \mu} \right) \frac{\partial E_x}{\partial y} \quad (28d)$$

Thus the longitudinal component of the Poynting vector

$$\overline{S} = \frac{1}{2} \overline{E} \times \overline{H}^* \quad (29)$$

(where $*$ denotes complex conjugation) is

$$S_z = \left(\frac{\beta}{2\omega \mu} \right) |E_x|^2 - \left(\frac{1}{2\omega \mu \beta} \right) E_x \frac{\partial^2 E_x^*}{\partial x^2} \quad (30)$$

It is observed from (28) that continuity of E_z and H_z across all horizontal and vertical cell boundaries in Figure 3 implies continuity of $\partial E_z/\partial x$ and $\partial E_x/\partial y$ across the same dielectric interfaces. Hence quasi-TE modes are the eigensolutions of the scalar Helmholtz equation

$$\nabla_T^2 E_x + k^2 E_x = \beta^2 E_x \quad (31)$$

with E_x continuous across all interfaces parallel to the horizontal xz plane but discontinuous across all interfaces parallel to the vertical yz plane.

A polarized five-point difference scheme will now be derived to approximate (31) at an internal grid point (x_r, y_s) where

$$k_{r,s} = k(x_r, y_s) \quad , \quad n_{r,s} = n(x_r, y_s) \quad , \quad E_{r,s} = E_x(x_r, y_s) \quad , \quad \text{etc}$$

At the interfaces between cells L and P , and between cells P and R in Figure 3, the principal field component E_x satisfies the discontinuity conditions

$$\varepsilon_L E_{r-1/2,s}^{(L)} = \varepsilon_P E_{r-1/2,s}^{(P)} \quad , \quad \varepsilon_P E_{r+1/2,s}^{(P)} = \varepsilon_R E_{r+1/2,s}^{(R)} \quad (32)$$

which, in view of (5), may be rewritten as

$$k_{r-1,s}^2 E_{r-1/2,s}^{(L)} = k_{r,s}^2 E_{r-1/2,s}^{(P)} \quad , \quad k_{r,s}^2 E_{r+1/2,s}^{(P)} = k_{r+1,s}^2 E_{r+1/2,s}^{(R)} \quad (33)$$

At these interfaces, $\partial E_x/\partial x$ satisfies the continuity conditions

$$\left(\frac{\partial E_x}{\partial x} \right)_{r-1/2,s}^{(L)} = \left(\frac{\partial E_x}{\partial x} \right)_{r-1/2,s}^{(P)} \quad , \quad \left(\frac{\partial E_x}{\partial x} \right)_{r+1/2,s}^{(P)} = \left(\frac{\partial E_x}{\partial x} \right)_{r+1/2,s}^{(R)} \quad (34)$$

It is now supposed that:

- (a) the field value $E_{r,s}$ in cell P "sees" a *spurious* field value $E_{r+1,s}^*$ in cell R (* does not refer to complex conjugation here), and
- (b) the field value $E_{r+1,s}$ in cell R "sees" a *spurious* field value $E_{r,s}^*$ in cell P .

By constructing the Taylor series

$$E_{r+1,s} = \sum_{m=0}^{\infty} \left(\frac{(h_x/2)^m}{m!} \right) \left(\frac{\partial^m E_x}{\partial x^m} \right)_{r+1/2,s}^{(R)} \quad (35a)$$

$$E_{r,s}^* = \sum_{m=0}^{\infty} \left(\frac{(-h_x/2)^m}{m!} \right) \left(\frac{\partial^m E_x}{\partial x^m} \right)_{r+1/2,s}^{(R)} \quad (35b)$$

$$E_{r+1,s}^* = \sum_{m=0}^{\infty} \left(\frac{(h_x/2)^m}{m!} \right) \left(\frac{\partial^m E_x}{\partial x^m} \right)_{r+1/2,s}^{(P)} \quad (35c)$$

$$E_{r,s} = \sum_{m=0}^{\infty} \left(\frac{(-h_x/2)^m}{m!} \right) \left(\frac{\partial^m E_x}{\partial x^m} \right)_{r+1/2,s}^{(P)} \quad (35d)$$

we find that

$$E_{r+1/2,s}^{(R)} = \frac{(E_{r+1,s} + E_{r,s}^*)}{2} + 0(h_x^2) \quad (36a)$$

$$h_x \left(\frac{\partial E_x}{\partial x} \right)_{r+1/2,s}^{(R)} = (E_{r+1,s} - E_{r,s}^*) + 0(h_x^3) \quad (36b)$$

$$E_{r+1/2,s}^{(P)} = \frac{(E_{r+1,s}^* + E_{r,s})}{2} + 0(h_x^2) \quad (37a)$$

$$h_x \left(\frac{\partial E_x}{\partial x} \right)_{r+1/2,s}^{(P)} = (E_{r+1,s}^* - E_{r,s}) + 0(h_x^3) \quad (37b)$$

By substituting (36a) and (37a) into (33), and (36b) together with (37b) into (34), we obtain

$$E_{r+1,s}^* = 2K_{r+1,s}^{(R)} E_{r+1,s} + \left(K_{r+1,s}^{(R)} - K_{r,s}^{(RP)} \right) E_{r,s} \quad (38)$$

in which

$$K_{r+1,s}^{(R)} = \frac{k_{r+1,s}^2}{k_{r,s}^2 + k_{r+1,s}^2} = \frac{n_{r+1,s}^2}{n_{r,s}^2 + n_{r+1,s}^2} \quad (39a)$$

$$K_{r+1,s}^{(RP)} = \frac{k_{r,s}^2}{k_{r,s}^2 + k_{r+1,s}^2} = \frac{n_{r,s}^2}{n_{r,s}^2 + n_{r+1,s}^2} \quad (39b)$$

It is next supposed that:

(c) the field value $E_{r,s}$ in cell P "sees" a *spurious* field value $E_{r-1,s}^{**}$ in cell L , and

(d) the field value $E_{r-1,s}$ in cell L "sees" a *spurious* field value $E_{r,s}^{**}$ in cell P .

Then a similar analysis to that given above causes (33) and (34) to yield

$$E_{r-1,s}^{**} = 2K_{r-1,s}^{(L)}E_{r-1,s} + \left(K_{r-1,s}^{(L)} - K_{r,s}^{(LP)}\right)E_{r,s} \quad (40)$$

where

$$K_{r,s}^{(LP)} = \frac{k_{r,s}^2}{k_{r-1,s}^2 + k_{r,s}^2} = \frac{n_{r,s}^2}{n_{r-1,s}^2 + n_{r,s}^2} \quad (41a)$$

$$K_{r-1,s}^{(L)} = \frac{k_{r-1,s}^2}{k_{r-1,s}^2 + k_{r,s}^2} = \frac{n_{r-1,s}^2}{n_{r-1,s}^2 + n_{r,s}^2} \quad (41b)$$

We are now able to form the approximations

$$\begin{aligned} h_x^2 \left(\frac{\partial^2 E_x}{\partial x^2} \right)_{r,s}^{(P)} &\approx E_{r-1,s}^{**} - 2E_{r,s} + E_{r+1,s}^* \\ &= 2K_{r-1,s}^{(L)}E_{r-1,s} \\ &\quad - \left(2 + \left(K_{r,s}^{(LP)} - K_{r-1,s}^{(L)} \right) + \left(K_{r,s}^{(RP)} - K_{r+1,s}^{(R)} \right) \right) E_{r,s} \\ &\quad + 2K_{r+1,s}^{(R)}E_{r+1,s} \\ &= 2K_{r-1,s}^{(L)}E_{r-1,s} - 2 \left(K_{r,s}^{(LP)} + K_{r,s}^{(RP)} \right) E_{r,s} \\ &\quad + 2K_{r+1,s}^{(R)}E_{r+1,s} \end{aligned} \quad (42a)$$

$$h_y^2 \left(\frac{\partial^2 E_x}{\partial y^2} \right)_{r,s}^{(P)} \approx E_{r,s-1} - 2E_{r,s} + E_{r,s+1} \quad (42b)$$

which may be substituted into the Helmholtz equation (31) to yield a five point difference scheme which reduces to the usual form (25), with E_x replacing E_z , when cells L , P , and R have the same refractive index. By applying the quasi-TE scheme at each internal grid point, with appropriate amendments when (x_r, y_s) is adjacent to the outer boundary of the modeled waveguide structure, we obtain the algebraic eigenvalue problem

$$A_{TE} \bar{E}_{TE} = \beta_{TE}^2 \bar{E}_{TE} \quad (43)$$

in which A_{TE} is a real *non-symmetric band* matrix, β_{TE}^2 is the quasi-TE propagation eigenvalue, and \bar{E}_{TE} is the corresponding normalized eigenvector representing the field profile $E_x(x, y)$.

5. Quasi-TM (E_y) Modes

Quasi-TM modes are defined by the laboratory polarization [7,14, 16,17,26]

$$\overline{E}(x, y, z, t) \equiv (0, E_y, E_z) \exp j(\omega t - \beta z) \quad (44)$$

which may be substituted into Maxwell's equations (3) to yield, in regions of piecewise constant refractive index,

$$E_z = - \left(\frac{j}{\beta} \right) \frac{\partial E_y}{\partial y} \quad (45a)$$

$$H_x = - \left(\frac{\beta}{\omega \mu} \right) E_y + \left(\frac{1}{\omega \mu \beta} \right) \frac{\partial^2 E_y}{\partial y^2} \quad (45b)$$

$$H_y = - \left(\frac{1}{\omega \mu \beta} \right) \frac{\partial^2 E_y}{\partial x \partial y} \quad (45c)$$

$$H_z = \left(\frac{j}{\omega \mu} \right) \frac{\partial E_y}{\partial x} \quad (45d)$$

The longitudinal component of the Poynting vector (29) now becomes

$$S_z = \left(\frac{\beta}{2\omega \mu} \right) |E_y|^2 - \left(\frac{1}{2\omega \mu \beta} \right) E_y \frac{\partial^2 E_y^*}{\partial y^2} \quad (45e)$$

(where * again denotes complex conjugation). Equations (45a) and (45d) show that $\partial E_y / \partial y$ and $\partial E_y / \partial x$ are continuous across all cell boundaries in Figure 3 due to the continuity of E_z and H_z across the same interfaces. Thus quasi-TM modes are eigensolutions of the scalar Helmholtz equation

$$\nabla_T^2 E_y + k^2 E_y = \beta^2 E_y \quad (46)$$

with E_y continuous across all interfaces parallel to the yz plane but discontinuous across all interfaces parallel to the xz plane.

The outline of a derivation for a five-point difference scheme to approximate equation (46) at an internal grid point (x_r, y_s) will now be given, where

$$k_{r,s} = k(x_r, y_s) \quad , \quad n_{r,s} = n(x_r, y_s) \quad , \quad E_{r,s} = E_y(x_r, y_s) \quad , \quad \text{etc}$$

At the interface between cell B and P in Figure 3, the principal field component E_y satisfies the conditions

$$k_{r,s-1}^2 E_{r,s-1/2}^{(B)} = k_{r,s}^2 E_{r,s-1/2}^{(P)} \quad , \quad \left(\frac{\partial E_y}{\partial y} \right)_{r,s-1/2}^{(B)} = \left(\frac{\partial E_y}{\partial y} \right)_{r,s-1/2}^{(P)} \quad (47)$$

whilst at the interface between cells P and A we have the relations

$$k_{r,s}^2 E_{r,s+1/2}^{(P)} = k_{r,s+1}^2 E_{r,s+1/2}^{(A)} \quad , \quad \left(\frac{\partial E_y}{\partial y} \right)_{r,s+1/2}^{(P)} = \left(\frac{\partial E_y}{\partial y} \right)_{r,s+1/2}^{(A)} \quad (48)$$

Then an analysis similar to that carried out for quasi-TE modes yields the approximations

$$\begin{aligned} h_y^2 \left(\frac{\partial^2 E_y}{\partial y^2} \right)_{r,s}^{(P)} &\approx 2K_{r,s-1}^{(B)} E_{r,s-1} \\ &\quad - \left(2 + \left(K_{r,s}^{(BP)} - K_{r,s-1}^{(B)} \right) + \left(K_{r,s}^{(AP)} - K_{r,s+1}^{(A)} \right) \right) E_{r,s} \\ &\quad + 2K_{r,s+1}^{(A)} E_{r,s+1} \\ &= 2K_{r,s-1}^{(B)} E_{r,s-1} - 2 \left(K_{r,s}^{(BP)} + K_{r,s}^{(AP)} \right) E_{r,s} \\ &\quad + 2K_{r,s+1}^{(A)} E_{r,s+1} \end{aligned} \quad (49a)$$

$$h_x^2 \left(\frac{\partial^2 E_y}{\partial x^2} \right)_{r,s}^{(P)} \approx E_{r-1,s} - 2E_{r,s} + E_{r+1,s} \quad (49b)$$

in which

$$K_{r,s+1}^{(A)} = \frac{k_{r,s+1}^2}{k_{r,s}^2 + k_{r,s+1}^2} = \frac{n_{r,s+1}^2}{n_{r,s}^2 + n_{r,s+1}^2} \quad (50a)$$

$$K_{r,s}^{(AP)} = \frac{k_{r,s}^2}{k_{r,s}^2 + k_{r,s+1}^2} = \frac{n_{r,s}^2}{n_{r,s}^2 + n_{r,s+1}^2} \quad (50b)$$

$$K_{r,s}^{(BP)} = \frac{k_{r,s}^2}{k_{r,s-1}^2 + k_{r,s}^2} = \frac{n_{r,s}^2}{n_{r,s-1}^2 + n_{r,s}^2} \quad (50c)$$

$$K_{r,s-1}^{(B)} = \frac{k_{r,s-1}^2}{k_{r,s-1}^2 + k_{r,s}^2} = \frac{n_{r,s-1}^2}{n_{r,s-1}^2 + n_{r,s}^2} \quad (50d)$$

The right hand sides of (49a) and (49b) may be substituted into the Helmholtz equation (46) to provide a five-point difference scheme

which reduces to the usual form (25), with E_y replacing E_z , when cells B , P , and A have the same refractive index. By using the quasi-TM scheme at each internal grid point, with appropriate amendments when (x_r, y_s) is adjacent to the outer boundary of the modeled waveguide structure, we obtain the algebraic eigenvalue problem

$$A_{\text{TM}} \bar{E}_{\text{TM}} = \beta_{\text{TM}}^2 \bar{E}_{\text{TM}} \quad (51)$$

in which A_{TM} is a real non-symmetric band matrix ($\neq A_{\text{TE}}$ in general), β_{TM}^2 is the quasi-TM propagation eigenvalue, and \bar{E}_{TM} is the corresponding normalized eigenvector storing the field profile $E_y(x, y)$.

6. H_y Modes

For H_y modes, which are analogous to quasi-TE modes [26], we consider the vertical polarization [8,14,16]

$$\bar{H}(x, y, z, t) \equiv (0, H_y, H_z) \exp j(\omega t - \beta z) \quad (52)$$

and then observe that Maxwell's equations (3) lead to

$$H_z = - \left(\frac{j}{\beta} \right) \frac{\partial H_y}{\partial y} \quad (53a)$$

$$E_x = \left(\frac{\beta}{\omega \epsilon} \right) H_y - \left(\frac{1}{\omega \epsilon \beta} \right) \frac{\partial^2 H_y}{\partial y^2} \quad (53b)$$

$$E_y = \left(\frac{1}{\omega \epsilon \beta} \right) \frac{\partial^2 H_y}{\partial x \partial y} \quad (53c)$$

$$E_z = - \left(\frac{j}{\omega \epsilon} \right) \frac{\partial H_y}{\partial x} \quad (53d)$$

The longitudinal component of the Poynting vector (29) now has the form

$$S_z = \left(\frac{\beta}{2\omega \epsilon} \right) |H_y|^2 - \left(\frac{1}{2\omega \epsilon \beta} \right) H_y^* \frac{\partial^2 H_y}{\partial y^2} \quad (54)$$

Thus these modes are eigensolutions of the equation

$$\nabla_T^2 H_y + k^2 H_y = \beta^2 H_y \quad (55)$$

with H_y and $\partial H_y / \partial y$ continuous across all cell boundaries in Figure 3, but with $\partial H_y / \partial x$ discontinuous across the same interfaces (where ε is discontinuous). However, the use of cell-centered grid points obviates the need to consider the discontinuity in $\partial H_y / \partial x$ across cell boundaries parallel to the xz plane.

Consideration will now be given to the derivation of a polarized five-point difference scheme to approximate (55) at an internal grid point (x_r, y_s) where

$$k_{r,s} = k(x_r, y_s) \quad , \quad n_{r,s} = n(x_r, y_s) \quad , \quad H_{r,s} = H_y(x_r, y_s) \quad , \quad \text{etc}$$

At the interfaces between cells L and P , and between cells P and R in Figure 3, the principal field component H_y satisfies the continuity conditions

$$H_{r-1/2,s}^{(L)} = H_{r-1/2,s}^{(P)} \quad , \quad H_{r+1/2,s}^{(P)} = H_{r+1/2,s}^{(R)} \quad (56)$$

whilst $\partial H_y / \partial x$ is subject to the discontinuity conditions

$$\left(\frac{1}{k_{r-1,s}^2} \right) \left(\frac{\partial H_y}{\partial x} \right)_{r-1/2,s}^{(L)} = \left(\frac{1}{k_{r,s}^2} \right) \left(\frac{\partial H_y}{\partial x} \right)_{r-1/2,s}^{(P)} \quad (57a)$$

$$\left(\frac{1}{k_{r,s}^2} \right) \left(\frac{\partial H_y}{\partial x} \right)_{r+1/2,s}^{(P)} = \left(\frac{1}{k_{r+1,s}^2} \right) \left(\frac{\partial H_y}{\partial x} \right)_{r+1/2,s}^{(R)} \quad (57b)$$

The derivation now proceeds in a similar manner to that adopted after equations (34) in Section 4, and will be included for completeness. It is supposed that:

(a) the field value $H_{r,s}$ in cell P "sees" a *spurious* value $H_{r+1,s}^*$ in cell R (* does not refer to complex conjugation here), and

(b) the field value $H_{r+1,s}$ in cell R "sees" a *spurious* value $H_{r,s}^*$ in cell P .

By constructing the Taylor series

$$H_{r+1,s} = \sum_{m=0}^{\infty} \left(\frac{(h_x/2)^m}{m!} \right) \left(\frac{\partial^m H_y}{\partial x^m} \right)_{r+1/2,s}^{(R)} \quad (58a)$$

$$H_{r,s}^* = \sum_{m=0}^{\infty} \left(\frac{(-h_x/2)^m}{m!} \right) \left(\frac{\partial^m H_y}{\partial x^m} \right)_{r+1/2,s}^{(R)} \quad (58b)$$

$$H_{r+1,s}^* = \sum_{m=0}^{\infty} \left(\frac{(h_x/2)^m}{m!} \right) \left(\frac{\partial^m H_y}{\partial x^m} \right)_{r+1/2,s}^{(P)} \quad (58c)$$

$$H_{r,s} = \sum_{m=0}^{\infty} \left(\frac{(-h_x/2)^m}{m!} \right) \left(\frac{\partial^m H_y}{\partial x^m} \right)_{r+1/2,s}^{(P)} \quad (58d)$$

we see that

$$H_{r+1,s}^{(R)} = \frac{(H_{r+1,s} + H_{r,s}^*)}{2} + O(h_x^2) \quad (59a)$$

$$h_x \left(\frac{\partial H_y}{\partial x} \right)_{r+1/2,s}^{(R)} = (H_{r+1,s} - H_{r,s}^*) + O(h_x^3) \quad (59b)$$

$$H_{r+1,s}^{(P)} = \frac{(H_{r+1,s}^* + H_{r,s})}{2} + O(h_x^2) \quad (60a)$$

$$h_x \left(\frac{\partial H_y}{\partial x} \right)_{r+1/2,s}^{(P)} = (H_{r+1,s}^* - H_{r,s}) + O(h_x^3) \quad (60b)$$

By substituting (59a) and (60a) into (56), and (59b) and (60b) into (57b), it is found that

$$H_{r+1,s}^* = 2K_{r,s}^{(RP)} H_{r+1,s} + \left(K_{r+1,s}^{(R)} - K_{r,s}^{(RP)} \right) H_{r,s} \quad (61)$$

where $K_{r+1,s}^{(R)}$ and $K_{r,s}^{(RP)}$ have the forms defined in (39a, b), and it should be noted that the coefficient of $H_{r+1,s}$ in (61) is not the same as that of $E_{r+1,s}$ in (38). It is next supposed that:

(c) the field value $H_{r,s}$ in cell P "sees" a *spurious* value $H_{r-1,s}^{**}$ in cell L , and

(d) the field value $H_{r-1,s}$ in cell L "sees" a *spurious* value $H_{r,s}^{**}$ in cell P .

Then a similar analysis to that performed above enables (56) and (57a) to yield

$$H_{r-1,s}^{**} = 2K_{r,s}^{(LP)} H_{r-1,s} + \left(K_{r-1,s}^{(L)} - K_{r,s}^{(LP)} \right) H_{r,s} \quad (62)$$

with $K_{r,s}^{(LP)}$ and $K_{r-1,s}^{(L)}$ having the forms given in (41), noting that the coefficient of $H_{r-1,s}$ in (62) is not that same as that of $E_{r-1,s}$ in

(40). It is now possible to form the approximations

$$\begin{aligned}
 h_x^2 \left(\frac{\partial^2 H_x}{\partial x^2} \right)_{r,s}^{(P)} &\approx H_{r-1,s}^{**} - 2H_{r,s} + H_{r+1,s}^* \\
 &= 2K_{r,s}^{(LP)} H_{r-1,s} \\
 &\quad - \left(2 + \left(K_{r,s}^{(LP)} - K_{r-1,s}^{(L)} \right) + \left(K_{r,s}^{(RP)} - K_{r+1,s}^{(R)} \right) \right) H_{r,s} \\
 &\quad + 2K_{r,s}^{(RP)} H_{r+1,s} \\
 &= 2K_{r,s}^{(LP)} H_{r-1,s} - 2 \left(K_{r,s}^{(LP)} + K_{r,s}^{(RP)} \right) H_{r,s} \\
 &\quad + 2K_{r,s}^{(RP)} H_{r+1,s}
 \end{aligned} \tag{63a}$$

$$h_y^2 \left(\frac{\partial^2 H_y}{\partial y^2} \right)_{r,s}^{(P)} \approx H_{r,s-1} - 2H_{r,s} + H_{r,s+1} \tag{63b}$$

which may be substituted into (55) to obtain a five-point difference scheme that reduces to the usual form (25), with H_y replacing E_z , when cells L , P , and R have identical refractive indices. The H_y scheme, when applied at each internal grid point, with appropriate modifications when (x_r, y_s) is adjacent to the outer boundary of the solution domain, generates the algebraic eigenvalue problem

$$A_{HY} \bar{H}_{HY} = \beta_{HY}^2 \bar{H}_{HY} \tag{64}$$

in which A_{HY} is a real non-symmetric band matrix, β_{HY}^2 is the H_y modal propagation eigenvalue, and \bar{H}_{HY} is the corresponding normalized eigenvector representing the field profile $H_y(x, y)$. It should be noted that A_{HY} is not identical to the quasi-TE finite difference matrix A_{TE} of Section 4.

7. H_x Modes

For H_x modes, which are analogous to quasi-TM modes [26], we consider the horizontal polarization [8,14,16]

$$\bar{H}(x, y, z, t) \equiv (H_x, 0, H_z) \exp j(\omega t - \beta z) \tag{65}$$

and then find from Maxwell's equations (3) that

$$H_z = - \left(\frac{j}{\beta} \right) \frac{\partial H_x}{\partial x} \quad (66a)$$

$$E_x = - \left(\frac{1}{\omega \epsilon \beta} \right) \frac{\partial^2 H_x}{\partial x \partial y} \quad (66b)$$

$$E_y = - \left(\frac{\beta}{\omega \epsilon} \right) H_x + \left(\frac{1}{\omega \epsilon \beta} \right) \frac{\partial^2 H_x}{\partial x^2} \quad (66c)$$

$$E_z = \left(\frac{j}{\omega \epsilon} \right) \frac{\partial H_x}{\partial y} \quad (66d)$$

The longitudinal component of the Poynting vector (29) takes the form

$$S_z = \left(\frac{\beta}{2\omega \epsilon} \right) |H_x|^2 - \left(\frac{1}{2\omega \epsilon \beta} \right) H_x^* \frac{\partial^2 H_x}{\partial x^2} \quad (67)$$

Hence these modes are eigensolutions of the scalar Helmholtz equation

$$\nabla_T^2 H_x + k^2 H_x = \beta^2 H_x \quad (68)$$

with H_x and $\partial H_x / \partial x$ continuous across all dielectric interfaces parallel to the xz and yz planes, but with $\partial H_x / \partial y$ discontinuous across these interfaces. However, the use of cell-centered grid points makes it unnecessary to consider the discontinuity of $\partial H_x / \partial y$ across cell boundaries parallel to the yz plane.

A brief derivation of a polarizaed five-point difference scheme to approximate (68) at an internal grid point (x_r, y_s) will now be presented, where

$$k_{r,s} = k(x_r, y_s) \quad , \quad n_{r,s} = n(x_r, y_s) \quad , \quad H_{r,s} = H_x(x_r, y_s) \quad , \quad \text{etc}$$

At the interface between cells B and P in Figure 3, the principal component H_x satisfies the conditions

$$\begin{aligned} H_{r,s-1/2}^{(B)} &= H_{r,s-1/2}^{(P)} \quad , \\ \left(\frac{1}{k_{r,s-1}^2} \right) \left(\frac{\partial H_x}{\partial y} \right)_{r,s-1/2}^{(B)} &= \left(\frac{1}{k_{r,s}^2} \right) \left(\frac{\partial H_x}{\partial y} \right)_{r,s-1/2}^{(P)} \end{aligned} \quad (69)$$

whilst at the interface between cells P and A , the corresponding relations are

$$H_{r,s+1/2}^{(P)} = H_{r,s+1/2}^{(A)},$$

$$\left(\frac{1}{k_{r,s}^2}\right) \left(\frac{\partial H_x}{\partial y}\right)_{r,s+1/2}^{(P)} = \left(\frac{1}{k_{r,s+1}^2}\right) \left(\frac{\partial H_x}{\partial y}\right)_{r,s+1/2}^{(A)} \quad (70)$$

Then an analysis similar to that carried out for H_y modes leads to the approximations

$$\begin{aligned} h_y^2 \left(\frac{\partial^2 H_x}{\partial y^2}\right)_{r,s}^{(P)} &\approx 2K_{r,s}^{(BP)} H_{r,s-1} \\ &\quad - \left(2 + \left(K_{r,s}^{(BP)} - K_{r,s-1}^{(B)}\right) + \left(K_{r,s}^{(AP)} - K_{r,s+1}^{(A)}\right)\right) H_{r,s} \\ &\quad + 2K_{r,s}^{(AP)} H_{r,s+1} \\ &= 2K_{r,s}^{(BP)} H_{r,s-1} - 2 \left(K_{r,s}^{(BP)} + K_{r,s}^{(AP)}\right) H_{r,s} \\ &\quad + 2K_{r,s}^{(AP)} H_{r,s+1} \end{aligned} \quad (71a)$$

$$h_x^2 \left(\frac{\partial^2 H_y}{\partial x^2}\right)_{r,s}^{(P)} \approx H_{r-1,s} - 2H_{r,s} + H_{r+1,s} \quad (71b)$$

where $K_{r,s+1}^{(A)}$, $K_{r,s}^{(AP)}$, $K_{r,s}^{(BP)}$, and $K_{r,s-1}^{(B)}$ are defined in (50a–d). The coefficients of $H_{r,s-1}$ and $H_{r,s+1}$ in (71a) are not the same as those of $E_{r,s-1}$ and $E_{r,s+1}$ in (49a). The right hand sides of (71a, b) may be substituted into (68) to produce a five-point difference scheme that will reduce to the usual form (25), with H_x replacing E_z , when cells A , P , and B have the same refractive index. When applied at each internal grid point, with appropriate amendments when (x_r, y_s) is adjacent to the outer boundary of the modeled waveguide structure, the H_x scheme gives rise to the algebraic eigenvalue equation

$$A_{HX} \bar{H}_{HX} = \beta_{HX}^2 \bar{H}_{HX} \quad (72)$$

in which A_{HX} is a real non-symmetric band matrix ($\neq A_{HY}$ in general), β_{HX}^2 is the H_x modal propagation eigenvalue, and \bar{H}_{HX} is the corresponding normalized eigenvector representing the field profile $H_x(x, y)$. It is observed that A_{HX} is not identical to the quasi-TM finite difference matrix A_{TM} of Section 5.

8. Finite Difference Matrices

The scalar Helmholtz equations (19), (31), (46), (55), and (68) may be summarized in the form

$$\nabla_T^2 F + k^2 F = \beta^2 F \quad (73)$$

For scalar modes, the eigenfunction $F(x, y)$ and its gradients $(\partial F/\partial x, \partial F/\partial y)$ are continuous throughout the modeled waveguide structure. In the case of semi-vectorial polarised modes, $F(x, y)$ represents one of the principal transverse \overline{E} -field or \overline{H} -field amplitude components which are required to satisfy appropriate continuity and discontinuity conditions across each cell boundary in Figure 3. The finite difference schemes established in Sections 3–7 convert equation (73) into the matrix eigenvalue problem

$$A\overline{F} = \beta^2 \overline{F} \quad (74)$$

where β^2 is the modal propagation eigenvalue and \overline{F} the corresponding normalized eigenvector representing the appropriate modal field profile $F(x, y)$. A is a real band matrix which is symmetric for scalar modes but non-symmetric for semi-vectorial polarised modes. In general, there is a different matrix A for each of the four polarised SVFD schemes derived in Sections 4–7.

When setting up the matrix A , the cell-centered finite difference grid (based on Figure 3) is scanned in a way which minimizes the band-width of A , with only the non-zero band being stored. This sloping band is converted into a rectangular array whose central column stores the principal diagonal of A , whilst the extreme left-hand column contains the lowest diagonal of the band and the extreme right-hand column holds the highest diagonal of the band. Furthermore, the grid scan takes full advantage of geometrical symmetry: it is only necessary to consider the right-hand (or left-hand) half of waveguide structures which possess left-right symmetry, as in Figures 1 and 2, and then apply boundary conditions along the vertical symmetry plane which are appropriate for even/symmetric or odd/antisymmetric modes. For symmetric modes $\partial F/\partial x = 0$ along the symmetry plane, whilst for antisymmetric modes $F(x, y) = 0$ along this plane (where $x = \text{constant}$). The finite difference grid is enclosed by an outer rectangular box boundary along which it is usual to impose either

(a) a closed boundary condition with zero values for the field profile $F(x, y)$ at all points provided the box is sufficiently large, or

(b) an open boundary condition with exponential decay of the field profile defined by

$$\frac{\partial F}{\partial \nu} = -(\beta^2 - k^2)^{1/2} F \quad (75)$$

where ν is the outward normal to the box boundary.

Obviously, the size of the box containing the grid is less critical for condition (b) than for (a). However, when the mode to be determined is close to cut-off, the box size must be sufficiently large for both conditions (a) and (b) in order to allow for the substantial field penetration into the cladding and/or substrate regions. As the decay constant in (75) depends on the (initially) unknown eigenvalue β^2 , condition (b) requires correction through a sequence of outer iterations superimposed over the inner iterations of the numerical method employed to solve the matrix eigenvalue problem (74). This involves updating the value of β used in the decay constant at the end of each cycle of inner iterations. Such a cycle forms one outer iteration for correcting the decay constant.

The matrix eigenvalue problem (74) may be solved by means of the shifted inverse power iteration method [45-48]

$$\overline{F}^{(m+1)} = (A - p^2 I)^{-1} \overline{F}^{(m)} \quad (76a)$$

used in the form

$$(A - p^2 I) \overline{F}^{(m+1)} = \overline{F}^{(m)} / \eta_m \quad (76b)$$

where p^2 is an initial estimate of β^2 , I is the unit matrix, and m ($= 0, 1, 2, 3, \dots$) is the iteration counter. η_m is chosen to normalize each $\overline{F}^{(m)}$ so that the latter's element of largest magnitude is equal to unity. The shifted matrix in (76b) is factorized into the product

$$A - p^2 I = LU \quad (77)$$

in which L and U are lower and upper triangular matrices, respectively. This factorization preserves the band-width of A and remains unchanged as the iteration counter m increases. The rectangular array that initially contains the non-zero band of the finite difference matrix A is overwritten by the above LU factorization, with the non-zero

band of L being stored in the left hand half of the array whilst the non-zero band of U is placed into right hand half of the array. Further details of the inverse power iteration method and the LU factorization technique are presented in Sections 9 and 10, respectively, where it is established that the iterative process (76) converges to the eigenvalue β^2 of A (together with its corresponding eigenvector) which is closer to the initial estimate p^2 than any other eigenvalue of this matrix. Thus, any required propagation mode (i.e., propagation constant plus related field profile) of a waveguide structure may be determined by choosing a suitable value for p^2 .

It is useful to estimate the array storage requirements of a computer program employing double precision arithmetic to solve the Helmholtz equation (73) via the matrix eigenvalue problem (74). For a modeled right-hand half waveguide box (or a full box if the structure does not possess left-right symmetry) covered by a grid with N_x horizontal and N_y vertical points, the computer memory requirement is

$$S_M \approx (4 + 2N_{min})(8N_xN_y) \text{ bytes} \quad (78a)$$

where

$$N_{min} = \min(N_x, N_y) \quad (78b)$$

with $2N_{min}(8N_xN_y)$ bytes being taken up by the rectangular array holding the non-zero band of the matrix A . So, for a grid with $N_x = 66$ and $N_y = 142$, the program would need nearly 10 megabytes, 97% of which would be used by the rectangular array storing the non-zero band of A . It should be noted that if advantage is not taken of the band structure of A , then the matrix would require $(8N_xN_y)^2$ bytes for double precision arithmetic (≈ 5600 megabytes with the quoted values of N_x and N_y).

In order to avoid the expensive computer memory requirements for storing the non-zero band of A , a Rayleigh quotient approach [9,14] for the SVFD solution of the Helmholtz equation (73) will be presented in Section 11. As this alternative technique does not involve the solution of a matrix eigenvalue problem, a vast amount of computer memory is "released" for other purposes, such as larger values of N_x and N_y together with smaller step lengths h_x and h_y for improved accuracy. However, there is a minor disadvantage in that the Rayleigh quotient can only be employed to determine the fundamental symmetric and leading antisymmetric modes of a waveguide structure

with left-right symmetry, whereas the matrix eigenvalue approach can be used to locate any required propagation mode.

9. Inverse Power Iteration Method

It is assumed that a square matrix A of order N has N distinct eigenvalues β_i^2 ($i = 1, 2, 3, \dots, N$) together with N corresponding eigenvectors \bar{F}_i . Real symmetric and complex Hermitian matrices possess this property which is probably also true, on physical grounds, for the real non-symmetric SVFD matrices of Sections 4–7. It is also assumed that any initial non-null vector $\bar{F}^{(0)}$ can be expressed as a linear combination of these eigenvectors, i.e.,

$$\bar{F}^{(0)} = \sum_{i=1}^N c_i \bar{F}_i \quad (79)$$

in which at least one of the scalar coefficients c_i is non-zero. Noting that

$$(A - p^2 I) \bar{F} = (\beta^2 - p^2) \bar{F} \quad (80a)$$

implies that

$$(A - p^2 I)^{-1} \bar{F} = (\beta^2 - p^2)^{-1} \bar{F} \quad (80b)$$

where I is the unit matrix and p^2 is an initial estimate to the required eigenvalue, the latter may be determined by employing the iterative process [45–48]

$$\bar{F}^{(m+1)} = (A - p^2 I)^{-1} \bar{F}^{(m)} = \sum_{i=1}^N \frac{c_i \bar{F}_i}{(\beta_i^2 - p^2)^{m+1}} \quad (81)$$

where $m (= 0, 1, 2, 3, \dots)$ is the iteration counter. It is next assumed that the β_i^2 are so ordered that

$$|\beta_i^2 - p^2| < |\beta_{i+1}^2 - p^2| \quad (i = 1, 2, 3, \dots, N-1) \quad (82)$$

which enables (81) to be rewritten in the form

$$\bar{F}^{(m+1)} = (\beta_1^2 - p^2)^{-(m+1)} \left(c_1 \bar{F}_1 + (\beta_1^2 - p^2)^{m+1} \sum_{i=2}^N \frac{c_i \bar{F}_i}{(\beta_i^2 - p^2)^{m+1}} \right) \quad (83)$$

For sufficiently large m , this becomes

$$\overline{F}^{(m+1)} = \frac{(c_1 \overline{F}_1 + \overline{e})}{(\beta_1^2 - p^2)^{m+1}} \quad (84)$$

in which the components of \overline{e} tend to zero, on account of the inequality (82). Hence

$$\overline{F}^{(m+1)} \rightarrow \frac{c_1 \overline{F}_1}{(\beta_1^2 - p^2)^{m+1}} \quad \text{as } m \rightarrow \infty \quad (85)$$

To ensure that the components of $\overline{F}^{(m+1)}$ converge to constant finite values as $m \rightarrow \infty$, a scaling factor $1/\eta_m$ is introduced into the iterative process (81), which then becomes

$$\overline{F}^{(m+1)} = \frac{(A - p^2 I)^{-1} \overline{F}^{(m)}}{\eta_m} = \frac{(\beta_1^2 - p^2)^{-1} \overline{F}^{(m)}}{\eta_m} \quad (86)$$

where η_m is chosen to normalize $\overline{F}^{(m)}$ so that the latter's element of largest magnitude is equal to unity. If the elements of $(\beta_1^2 - p^2) \overline{F}^{(m+1)}$ are to converge to those of $\overline{F}^{(m)}/\eta_m$ as m increases, we must have

$$\eta_m \rightarrow \frac{1}{(\beta_1^2 - p^2)} \quad \text{as } m \rightarrow \infty \quad (87a)$$

which yields

$$\beta_1^2 \rightarrow p^2 + \frac{1}{\eta_m} \quad \text{as } m \rightarrow \infty \quad (87b)$$

where β_1^2 is the eigenvalue of A that is closer to the initial estimate p^2 than are the other $(N-1)$ eigenvalues β_i^2 ($i = 2, 3, 4, \dots, N$) by virtue of the inequality (82). The converged normalized vector $\overline{F}^{(m)}/\eta_m$ is regarded as the corresponding eigenvector \overline{F}_1 .

In order to preserve the band structure of $(A - p^2 I)$, the iterative process (86) is normally employed in the form

$$(A - p^2 I) \overline{F}^{(m+1)} = \overline{F}^{(m)}/\eta_m \quad (m = 0, 1, 2, 3, \dots) \quad (88)$$

because the inverse of a band matrix is usually dense which would thereby considerably increase computer memory requirements. The shifted matrix $(A - p^2 I)$ is factorized into the product

$$A - p^2 I = LU \quad (89)$$

where L is a lower triangular matrix with unit elements on its principal diagonal and U is an upper triangular matrix. (This factorization remains unchanged as m increases). Each iteration $m (= 0, 1, 2, 3, \dots)$ then requires the solution of the two triangular systems of linear algebraic equations

$$L\bar{G}^{(m)} = \bar{F}^{(m)} / \eta_m, \quad U\bar{F}^{(m+1)} = \bar{G}^{(m)} \quad (90)$$

to update the estimates to β_1^2 and the corresponding normalized eigenvector $\bar{F}^{(m+1)}$. The LU factorization is described in the following section.

10. Triangular Factorization of a Matrix

Given that

$$\tilde{A} = A - p^2 I \quad (91)$$

is a square matrix of order N , then it can be factorized into the product [45,47,48]

$$\tilde{A} = LU \quad (92)$$

in which L and U are lower and upper triangular matrices of order N , respectively. Let the elements of \tilde{A} , L , and U be a_{im} , ℓ_{im} , and u_{im} ($i, m = 1, 2, \dots, N$), respectively. Now \tilde{A} has N^2 known elements whilst L and U contain a total of $(N^2 + N)$ unknown elements. It is therefore usually convenient to choose the N arbitrary values

$$\ell_{ii} = 1 \quad \text{for } i = 1, 2, 3, \dots, N \quad (93)$$

It is then observed that row 1 in the product (92) yields

$$u_{1m} = a_{1m} \quad \text{for } m = 1, 2, 3, \dots, N \quad (94)$$

By matrix multiplication, it is found that the elements in row i ($= 2, 3, \dots, N$) of L and U are given by

$$\ell_{im} = \frac{\left(a_{im} - \sum_{q=1}^{m-1} \ell_{iq} u_{qm} \right)}{u_{mm}} \quad (95a)$$

for columns $m = 1, 2, 3, \dots, (i-1)$ and

$$u_{im} = a_{im} - \sum_{q=1}^{i-1} \ell_{iq} u_{qm} \quad (95b)$$

for columns $m = i, i+1, i+2, \dots, N$.

It should be noted that, when \tilde{A} is a band matrix, the triangular factorization (92) preserves the bandwidth of \tilde{A} .

11. Rayleigh Quotient Solution

The classical Rayleigh quotient solution of the matrix eigenvalue problem (74) is [14,45-48]

$$\beta^2 = \frac{(\overline{F}^T A \overline{F})}{(\overline{F}^T \cdot \overline{F})} \quad (96)$$

where the superscript T denotes the transpose of a matrix or of a column vector. The corresponding Rayleigh quotient solution of the Helmholtz equation (73) is [1,3,9,16,19,26,49]

$$\begin{aligned} \beta^2 &= \frac{\iint_S F (\nabla_T^2 F + k^2 F) dx dy}{\iint_S F^2 dx dy} \\ &= \frac{\iint_S (k^2 F^2 - (\nabla_T F)^2) dx dy}{\iint_S F^2 dx dy} \end{aligned} \quad (97)$$

in which the double integrals are evaluated over the cross-section S of the modeled right-hand half (or full) waveguide box. Iterations of the Rayleigh quotient (96) are guaranteed to converge only when A is a real symmetric (or complex Hermitian) matrix. (They may or may not converge when A is non-symmetric). Similarly, this guarantee of convergence applies to the Rayleigh quotient (97) only when $F(x, y)$ and its gradients are continuous throughout S , i.e., for scalar unpolarized modes.

To ensure convergence of Rayleigh quotient iterations for semi-vectorial polarised modes, the matrix eigenvalue problem (74) is symmetrized by forming the product [9,14]

$$\overline{F}^T A^T A \overline{F} = (\beta^2 \overline{F}^T) \cdot (\beta^2 \overline{F}) \quad (98a)$$

from which we obtain, for a given approximation to \overline{F} ,

$$(\beta^2)^2 = (\overline{F}^T A^T A \overline{F}) / (\overline{F}^T \cdot \overline{F}) \quad (98b)$$

Application of this symmetrization process to equation (73) yields the Rayleigh quotient [9,14]

$$(\beta^2)^2 = \frac{\iint (\nabla_T^2 F + k^2 F)^2 dx dy}{\iint_S F^2 dx dy} \quad (99)$$

for an estimated field profile $F(x, y)$ which represents any of the principal transverse \overline{E} -field or \overline{H} -field amplitude components defined in Sections 4–7 above. For a given numerical approximation to $F(x, y)$, the numerator integrand in (99) is approximated at each grid point within S by employing the appropriate SVFD scheme from one of the Sections 4–7. It should be noted that the integrands in the numerator and denominator are both positive at all points in S ; this property is highly desirable for numerical stability because no cancellations will occur during the process of numerical integration. On the other hand, the numerator integrand of equation (97) is not guaranteed to be positive at all grid points within the domain of integration.

After an estimate of β^2 has been computed via equation (99), the field profile is updated from an iterative solution of the system of

linear algebraic equations (74) rewritten in the diagonally dominant form

$$\tilde{A}\bar{F} = (A - k^2 I)\bar{F} = (\beta^2 - k^2)\bar{F} \quad (100)$$

where I is the unit matrix and $\tilde{A}F$ represents the appropriate polarised finite difference approximation for $\nabla_T^2 F$. Application of the successive over-relaxation (SOR) method [45,47,48,50-52] to this latter system at an internal grid point (x_r, y_s) leads to the iterative scheme (see Figure 3)

$$\begin{aligned} F_{r,s}^{(m+1)} = & [(1 - \eta) + (\eta/a_P)(\beta^2 - k^2)] F_{r,s}^{(m)} \\ & - (\eta/a_P) [a_B F_{r,s-1}^{(m+1)} + a_L F_{r-1,s}^{(m+1)} + a_R F_{r+1,s}^{(m)} + a_A F_{r,s+1}^{(m)}] \end{aligned} \quad (101)$$

in which η is the relaxation factor and $m (= 0, 1, 2, 3, \dots)$ is the iteration counter. The coefficients a_B , a_L , a_P , a_R , and a_A depend on position and the chosen SVFD scheme. Equation (101) is written in a form which assumes that each internal grid row s is scanned from left to right, starting with the bottom row and ending with the top row. The outer box boundary conditions employed with (99) and (101) are the same as those considered in Section 8 under (a) and (b), the latter involving (75).

In terms of the notation defined in the paragraph of section 8 containing (78), the array storage requirement of a double precision computer program, based on the Rayleigh quotient and SOR methods of equations (99) and (101), is

$$S_R \approx 4(8N_x N_y) \approx S_M - 2N_{min}(8N_x N_y) \text{ bytes} \quad (102)$$

so that

$$\frac{S_M}{S_R} \approx 1 + \frac{N_{min}}{2} \quad (103)$$

Hence, for the case $N_{min} = 66$ considered in Section 8, $S_M \approx 34S_R$.

It should be noted that the iterations of the Rayleigh quotient (99) will always converge to either the fundamental symmetric or leading antisymmetric mode of the polarization under consideration, depending on the form of boundary condition applied along the vertical symmetry plane, as mentioned in Section 8. On the other hand, solutions of the matrix eigenvalue equation (74) will converge to any desired

propagation mode, as established in Section 9, but with the computer memory penalty given by the estimates (78), (102), and (103). The very economical storage requirements of equations (99) and (101), relative to those of (74), can be exploited to substantially increase the number of available grid points, coupled with smaller step lengths, so that propagation constants and associated field profiles may be computed with greater accuracy.

The following section contains brief descriptions of three well known iterative methods (including SOR) for solving systems of simultaneous linear algebraic equations of the form (100).

12. Iterative Methods for Linear Algebraic Equations

This section provides brief outlines of three familiar iterative methods which may be employed to solve systems of simultaneous linear algebraic equations of the form

$$\tilde{A}\overline{F} = \overline{b} \quad (104a)$$

where, from equation (100),

$$\tilde{A} = A - k^2 I \quad \text{and} \quad \overline{b} = (\beta^2 - k^2)\overline{F} \quad (104b)$$

\tilde{A} , \overline{F} , and \overline{b} have elements a_{im} , f_i , and b_i ($i, m = 1, 2, 3, \dots, N$), respectively.

(i) The simplest of iterative techniques for solving the system (104) is the Jacobi method which is given by [45,47,48]

$$f_i^{(q+1)} = \frac{1}{a_{ii}} \left(b_i - \sum_{m=1}^{i-1} a_{im} f_m^{(q)} - \sum_{m=i+1}^N a_{im} f_m^{(q)} \right) \quad (105)$$

($i = 1, 2, 3, \dots, N$) where q ($= 0, 1, 2, 3, \dots$) is the iteration counter and $\overline{F}^{(0)}$ is the initial approximation to the solution \overline{F} . Convergence of the iterations is guaranteed when the matrix \tilde{A} is diagonally dominant, i.e.,

$$|a_{ii}| > \sum_{m=1}^{i-1} |a_{im}| + \sum_{m=i+1}^N |a_{im}| \quad (106)$$

for $i = 1, 2, 3, \dots, N$.

(ii) The Gauss-Seidel method, which is a modification of the Jacobi iterative scheme (105), is given by [45,47,48]

$$f_i^{(q+1)} = \frac{1}{a_{ii}} \left(b_i - \sum_{m=1}^{i-1} a_{im} f_m^{(q+1)} - \sum_{m=i+1}^N a_{im} f_m^{(q)} \right) \quad (107)$$

for $i = 1, 2, 3, \dots, N$ and $q = 0, 1, 2, 3, \dots$. Convergence is again guaranteed if the elements of \bar{A} satisfy the diagonal dominance inequality (106). The rate of convergence of (107) is then at least twice that of (105).

(iii) The amount by which the approximation to the solution \bar{F} of equation (104) changed during one Gauss-Seidel iteration is determined by rewriting (107) in the form

$$f_i^{(q+1)} - f_i^{(q)} = \frac{1}{a_{ii}} \left(b_i - \sum_{m=1}^{i-1} a_{im} f_m^{(q+1)} - \sum_{m=i}^N a_{im} f_m^{(q)} \right) \quad (108)$$

In the successive over-relaxation (SOR) method, this change in the approximation to \bar{F} is accelerated by multiplying the right-hand side of (108) with a positive real number η , called the relaxation factor, to obtain the iterative scheme [45,48,50–52]

$$f_i^{(q+1)} = (1-\eta) f_i^{(q)} + \frac{\eta}{a_{ii}} \left(b_i - \sum_{m=1}^{i-1} a_{im} f_m^{(q+1)} - \sum_{m=i+1}^N a_{im} f_m^{(q)} \right) \quad (109)$$

for $i = 1, 2, 3, \dots, N$ and $q = 0, 1, 2, 3, \dots$. The SOR iterations will converge provided the relaxation factor lies in the range

$$0 < \eta < 2 \quad (110)$$

and the elements of \bar{A} satisfy (106). It should be noted that (109) reduces to (107) when $\eta = 1$.

Any of the above three iterative methods will also converge whenever the spectral radius (the modulus of the dominant eigenvalue) of its respective iteration matrix (derived from \bar{A}) is strictly less than unity [45,50,51]. This is a necessary condition for convergence, whereas the diagonal dominance inequality (106) is a sufficient condition.

13. Numerical Results for Single Rib Waveguides

After computing any modal eigenvalue β^2 of a waveguide structure, by solving either equation (74) via (76b) and (77) or the pair of equations (99) and (101), it is useful to calculate the modal index

$$\eta_{eff} = \frac{\beta}{k_0} \quad \text{where} \quad k_0 = \frac{2\pi}{\lambda} \quad (111)$$

and the normalized index

$$b = \frac{n_{eff}^2 - n_s^2}{n_G^2 - n_s^2} \quad (112)$$

(see Figs. 1 and 2 for notation). For propagation, we require

$$n_s \leq n_{eff} \leq n_G \quad , \quad 0 \leq b < 1 \quad (113)$$

assuming that $n_s \geq n_c$, otherwise n_c should replace n_s in (112) and (113). The matrix eigenvalue and Rayleigh quotient approaches have been tested on various rib waveguide structures [7-9,14], and many of these results will be reproduced here together with more detailed contour plots of semi-vectorial field profiles (at 10%, instead of the previous 20%, intervals of the maximum field amplitude).

	n_G	n_s	n_c	W μm	H μm	D μm	X_s μm	Y_s μm	Y_c μm	h_x μm	h_y μm
BT1	3.44	3.34	1.0	2	1.1	0.2	3.00	5.025	0.525	0.0952	0.05
BT2	3.44	3.36	1.0	3	0.1	0.9	3.05	5.025	0.525	0.0968	0.05
BT3	3.44	3.435	1.0	4	2.5	3.5	4.34	7.550	0.550	0.0976	0.10

Table 1. The semiconductor rib waveguide structures BT1, BT2, and BT3 from Refs. [3,7,8]. (See Figs. 1 and 3 for notation.) The wavelength considered was $\lambda = 1.55\mu\text{m}$. (©IEE [7,8] 1988)

Boundary condition	Zero field on the outer box boundary	Exponential decay on the outer box boundary
Structure	n_{eff} : b	n_{eff} : b
BT1	3.3901676 : 0.4979888	3.3901676 : 0.4979888
BT2	3.3954801 : 0.4406	3.3955255 : 0.4412
BT3	3.4367069 : 0.3412	3.4368442 : 0.3687

Table 2A. Fundamental symmetric scalar modes for the rib waveguide structures of Ref. [3] and Table 1 with $\lambda = 1.55\mu\text{m}$. (©IEE [7] 1988)

Boundary condition	Zero field on the outer box boundary	Exponential decay on the outer box boundary
Structure	n_{eff} : b	n_{eff} : b
T1	3.3869266 : 0.4655926	3.3869266 : 0.4655926
BT2	3.3953942 : 0.4395	3.3954405 : 0.4401
BT3	3.4366674 : 0.3333	3.4368112 : 0.3621

Table 2B. Fundamental symmetric quasi-TE modes for the rib waveguide structures of Ref. [3] and Table 1 with $\lambda = 1.55\mu\text{m}$. (©IEE [7] 1988)

Boundary condition	Zero field on the outer box boundary	Exponential decay on the outer box boundary
Structure	n_{eff} : b	n_{eff} : b
BT1	3.3867447 : 0.4637752	3.3867447 : 0.4637751
BT2	3.3905538 : 0.3792	3.3905927 : 0.3796
BT3	3.4366376 : 0.3274	3.4367719 : 0.3542

Table 2C. Fundamental symmetric quasi-TM modes for the rib waveguide structures of Ref. [3] and Table 1 with $\lambda = 1.55\mu\text{m}$. (©IEE [7] 1988)

	H_y mode	H_x mode
Structure	n_{eff} : b	n_{eff} : b
BT1	3.3869266 : 0.4655926	3.3867447 : 0.4637751
BT2	3.3954405 : 0.4401	3.3905927 : 0.3796
BT3	3.4368121 : 0.3623	3.4367729 : 0.3544

Table 3. Fundamental symmetric H-field modes for the rib waveguide structures of Refs. [3,7] and Table 1. ($\lambda = 1.55\mu\text{m}$.) The outer box boundary condition was iteratively corrected exponential decay of field profiles. (©IEE [8] 1988)

We first consider the three rib waveguides (BT1, BT2, BT3) originally analyzed in reference [3] and subsequently examined in [7,8,14,30, 53–56]. Their optical and geometrical parameters are specified in Table 1, whilst values of the modal and normalized indices, as determined via the matrix eigenvalue method, for their fundamental symmetric quasi-TE, quasi-TM, and scalar modes appear in Tables 2(A,B,C). Matrix eigenvalue results for the corresponding semi-vectorial \overline{H} -field modes are presented in Table 3. It is observed that corresponding \overline{E} -field and \overline{H} -field indices are identical (with very minor differences for the weakly guiding structure BT3). It is seen that the choice of outer box boundary conditions does not affect the computed values of η_{eff} and b for the strongly guiding structure BT1, but that it does produce changes (in the expected direction) for the weaker guiding structures BT2 and BT3. All of these results lie within the range of values quoted by other authors [3,30,53–56]. Contour and surface plots of the fundamental quasi-TE field profile within each structure (with iteratively corrected exponential decay on the outer box boundary) are displayed in Figures 4(A,B), 5(A,B), and 6(A,B).

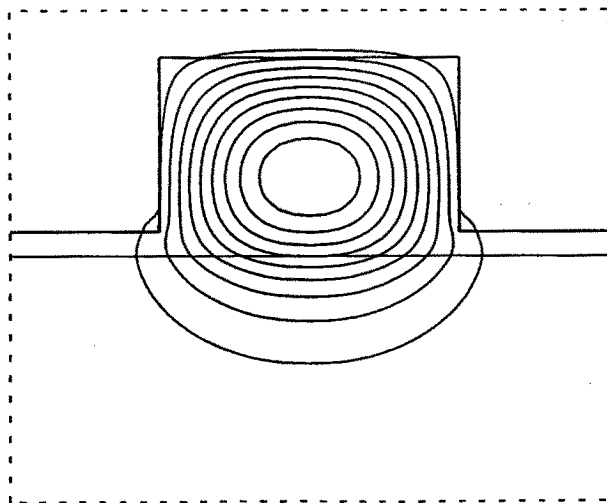


Figure 4A. Fundamental symmetric quasi-TE field profile within the structure BT1 of reference [3] and Table 1. Contour levels are at 10% intervals of the maximum field amplitude. ($\lambda = 1.55\mu\text{m}$) Note the slight discontinuity in E_x across vertical dielectric interfaces.

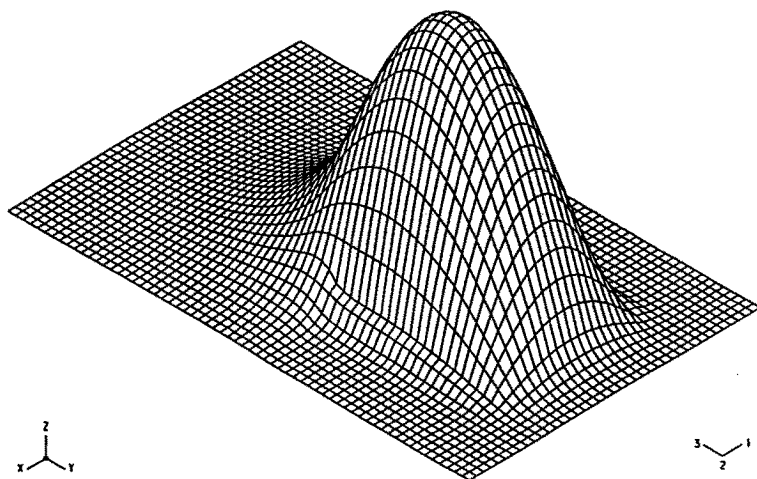


Figure 4B. Fundamental symmetric quasi-TE field profile within the structure BT1 of reference [3] and Table 1 when $\lambda = 1.55\mu\text{m}$. (©IEE [7] 1988)

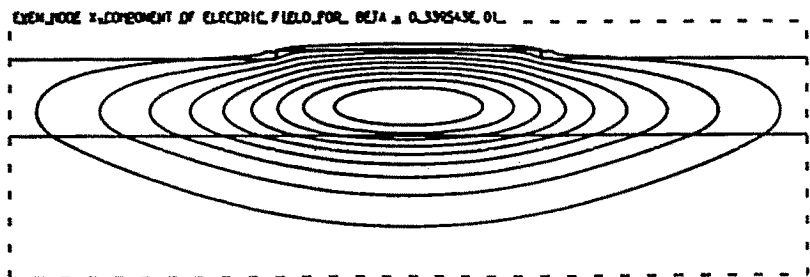


Figure 5A. Fundamental symmetric quasi-TE field profile within the structure BT2 of reference [3] and Table 1. Contour levels are at 10% intervals of the maximum field amplitude. ($\lambda = 1.55\mu\text{m}$) Note the slight discontinuity in E_x across vertical dielectric interfaces.

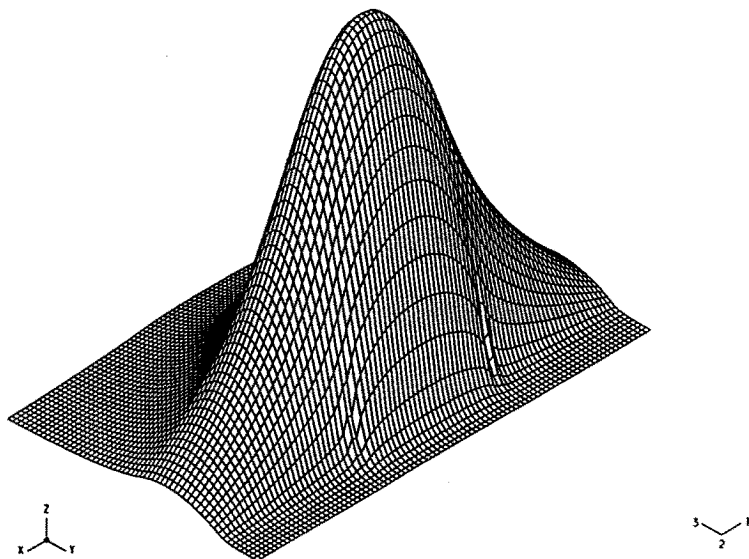


Figure 5B. Fundamental symmetric quasi-TE field profile within the structure BT2 of reference [3] and Table 1 when $\lambda = 1.55\mu\text{m}$. (©IEE [7] 1988)

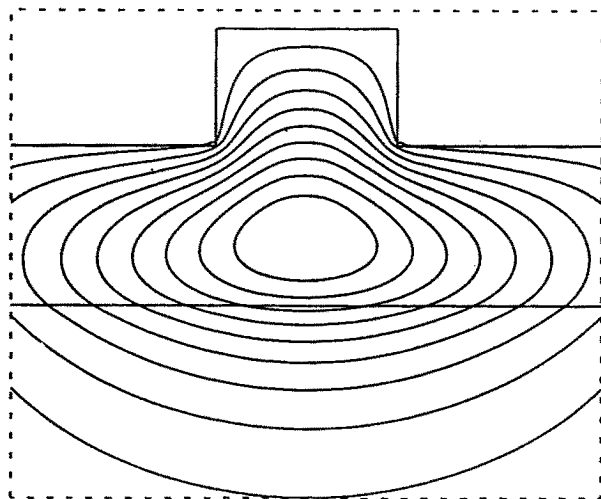


Figure 6A. Fundamental symmetric quasi-TE field profile within the structure BT3 of reference [3] and Table 1. Contour levels are at 10% intervals of the maximum field amplitude. ($\lambda = 1.55\mu\text{m}$) Note the slight discontinuity in E_x across vertical dielectric interfaces.

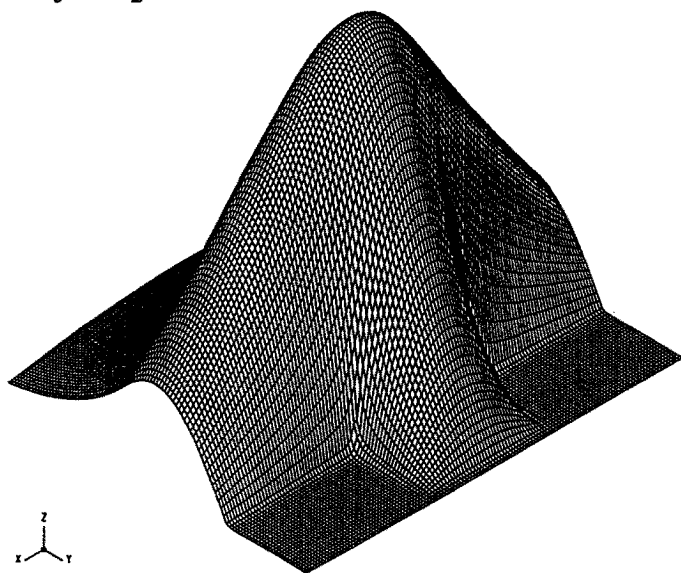


Figure 6B. Fundamental symmetric quasi-TE field profile within the structure BT3 of reference [3] and Table 1 when $\lambda = 1.55\mu\text{m}$. (©IEE [7] 1988)

When the Rayleigh quotient method, with iteratively corrected exponential decay on the outer box boundary, was applied to the waveguides BT1, BT2 and BT3 with the same parameters as listed in Table 1, it yielded the same polarised indices as reported in Tables 2(B,C) and 3 for the matrix eigenvalue approach. However, revised results for these three structures, with their box parameters modified to those shown in Table 4, have been obtained via the Rayleigh quotient technique with horizontal and vertical step lengths five times smaller than those employed previously; the revised indices are presented in Table 5.

	n_g	n_s	n_c	W μm	H μm	D μm	X_s μm	Y_s μm	Y_c μm	h_x μm	h_y μm
BT1	3.44	3.34	1.0	2	1.1	0.2	1.00	1.505	0.305	0.0198	0.01
BT2	3.44	3.36	1.0	3	0.1	0.9	2.99	1.505	0.305	0.01987	0.01
BT3	3.44	3.435	1.0	4	2.5	3.5	4.49	4.010	0.310	0.0199	0.02

Table 4. The semiconductor rib waveguide structures BT1, BT2, and BT3 from Refs. [3,7,8,14]. (See Figs. 1 and 3 for notation.) The wavelength considered was $\lambda = 1.55\mu\text{m}$. (©IEE [14] 1991)

	Quasi-TE	Quasi-TM
Structure	n_{eff} : b	n_{eff} : b
BT1	3.3882623 : 0.4789	3.3875430 : 0.4718
BT2	3.3952147 : 0.4373	3.3905701 : 0.3794
BT3	3.4368064 : 0.3611	3.4367751 : 0.3549

Table 5. Fundamental symmetric modes for the rib waveguide structures of Refs [3,7,8,14] and Table 4. ($\lambda = 1.55\mu\text{m}$.) The outer box boundary condition was iteratively corrected exponential decay of field profiles. (©IEE [14] 1991)

Attention will now be paid to the GaAs/GaAlAs rib waveguide structure UCL1 which was originally considered in references [36,57,58] and subsequently analyzed in [7-9,14,18,23-30,49,53,54,59-66]. Its optical and geometrical parameters are listed in Table 6, whilst its fundamental symmetric semivectorial \overline{E} -field and \overline{H} -field modal and normalized indices, as determined by the matrix eigenvalue approach, are presented in Table 7 as a function of the outer slab thickness D which varies from 0 to $1\mu\text{m}$ (with the rib height correspondingly varying from 1 to $0\mu\text{m}$). The leading antisymmetric polarised indices, obtained by the same method, appear in Table 8. Contour and surface plots of the fundamental symmetric and leading antisymmetric quasi-TE field profiles are displayed in Figures 7(A,B) and 8(A,B), respectively, for the case $D = H = 0.5\mu\text{m}$ (in the notation of Figure 1). The Rayleigh quotient method, with iteratively corrected exponential decay on the outer box boundary, yielded the same results as those of Table 7 when used with the parameters given in Table 6. Revised values of the semivectorial polarised indices, obtained via (99) and (101) with the modified box and grid parameters shown in Table 9, may be found in Tables 10 and 11. It should be noted that the SVFD-TE results of Tables 7 and 10 are in close agreement with corresponding vector \overline{H} -field finite element (VFE) values, displayed on a diagram in [36], which have been reproduced in references [49,64,66]. (The VFE-TE indices quoted in [7,9] contained some small reading errors which were subsequently corrected).

n_g	n_s	n_c	W μm	$H+D$ μm	X_s μm	Y_s μm	Y_c μm	h_x μm	h_y μm
3.44	3.40	1.0	3	1	2.952	5.025	1.025	0.0968	0.05

Table 6. The GaAs/Ga_{0.9}Al_{0.1}As rib waveguide structure UCL1 from Refs. [7-9,14,36,57,58]. (See Figs. 1 and 3 for notation.) The wavelength considered was $\lambda = 1.15\mu\text{m}$. (©IEE [7,8] 1988)

D :		E_x and H_y		:	E_y and H_x	
μm :	n_{eff}	:	b	:	n_{eff}	b
0.0 :	3.41188	:	0.2959	:	3.41051	0.2617
0.1 :	3.41200	:	0.2987	:	3.41060	0.2639
0.2 :	3.41217	:	0.3029	:	3.41073	0.2672
0.3 :	3.41240	:	0.3088	:	3.41092	0.2718
0.4 :	3.41271	:	0.3165	:	3.41117	0.2780
0.5 :	3.41310	:	0.3263	:	3.41150	0.2862
0.6 :	3.41358	:	0.3382	:	3.41190	0.2964
0.7 :	3.41415	:	0.3524	:	3.41241	0.3089
0.8 :	3.41484	:	0.3696	:	3.41303	0.3245
0.9 :	3.41568	:	0.3905	:	3.41385	0.3448
1.0 :	3.41733	:	0.4319	:	3.41551	0.3863

Table 7. Fundamental symmetric E-field and H-field modes for the structure UCL1 of Refs. [7-9,36,57,58] and Table 6. ($\lambda = 1.15\mu\text{m}$.) The outer box boundary condition was iteratively corrected exponential decay of field profiles. (©IEE [7,8] 1988)

D :		Quasi-TE		:	Quasi-TM	
μm :	n_{eff}	:	b	:	n_{eff}	b
0.35:	3.40026	:	0.0065	:		
0.4 :	3.40094	:	0.0235	:	3.40006	0.0016
0.45:	3.40173	:	0.0431	:	3.40065	0.0162
0.5 :	3.40262	:	0.0652	:	3.40137	0.0341
0.6 :	3.40471	:	0.1171	:	3.40312	0.0776
0.7 :	3.40720	:	0.1792	:	3.40532	0.1323
0.75:	3.40858	:	0.2136	:	3.40659	0.1640

Table 8. Leading antisymmetric modes for the structure UCL1 of Refs. [7-9, 14,36,57,58] and Table 6. ($\lambda = 1.15\mu\text{m}$.) The outer box boundary condition was iteratively corrected exponential decay of field profiles. These modes are cut-off by the outer slab modes when $D > 0.75\mu\text{m}$. (©IEE [30] 1990)

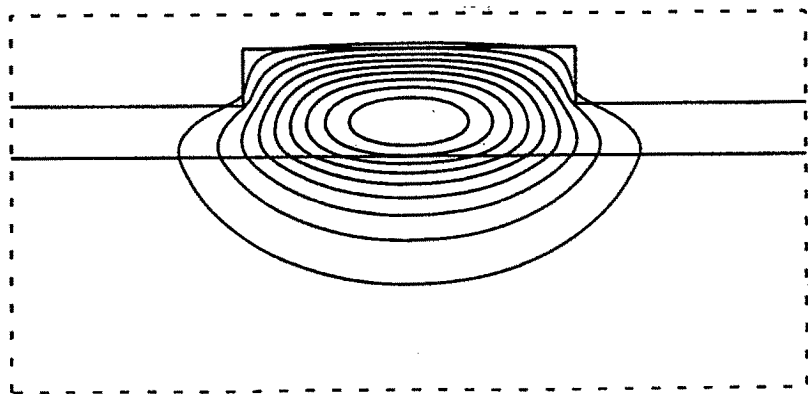


Figure 7A. Fundamental symmetric quasi-TE field profile within the structure UCL1 of reference [36] and Table 6, when $D = H = 0.5\mu\text{m}$ and $\lambda = 1.15\mu\text{m}$. Contour levels are at 10% intervals of the maximum field amplitude. Note the slight discontinuity in E_x across vertical dielectric interfaces.

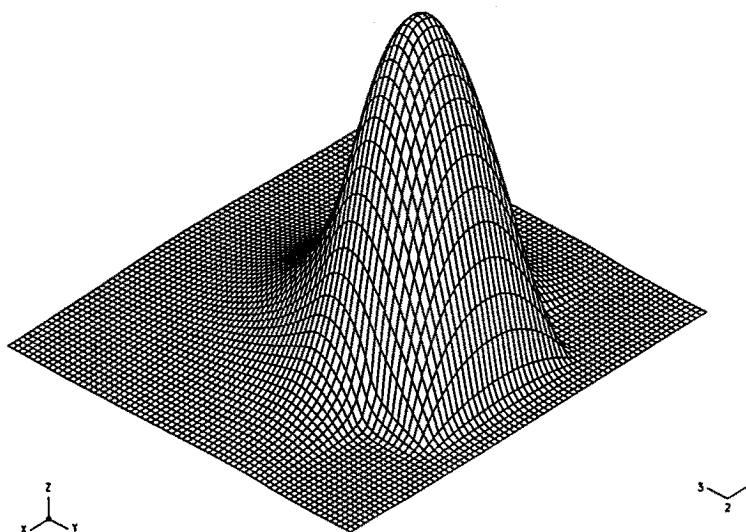


Figure 7B. Fundamental symmetric quasi-TE field profile within the structure UCL1 of reference [36] and Table 6, when $D = H = 0.5\mu\text{m}$ and $\lambda = 1.15\mu\text{m}$.

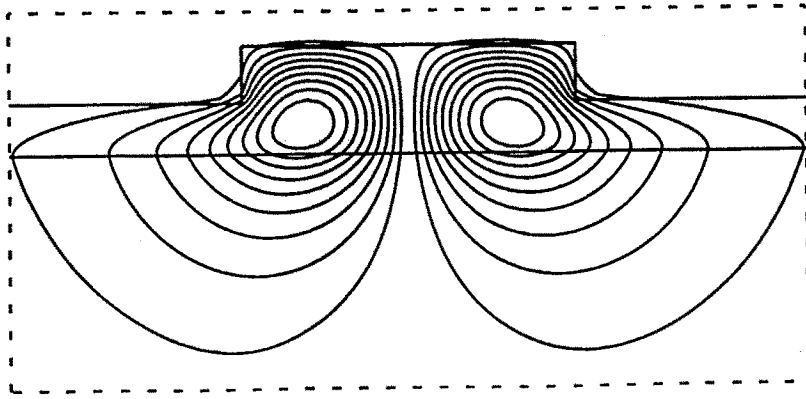


Figure 8A. Leading antisymmetric quasi-TE field profile within the structure UCL1 of reference [36] and Table 6, when $D = H = 0.5\mu\text{m}$ and $\lambda = 1.15\mu\text{m}$. Contour levels are at 10% intervals of the maximum field amplitude.

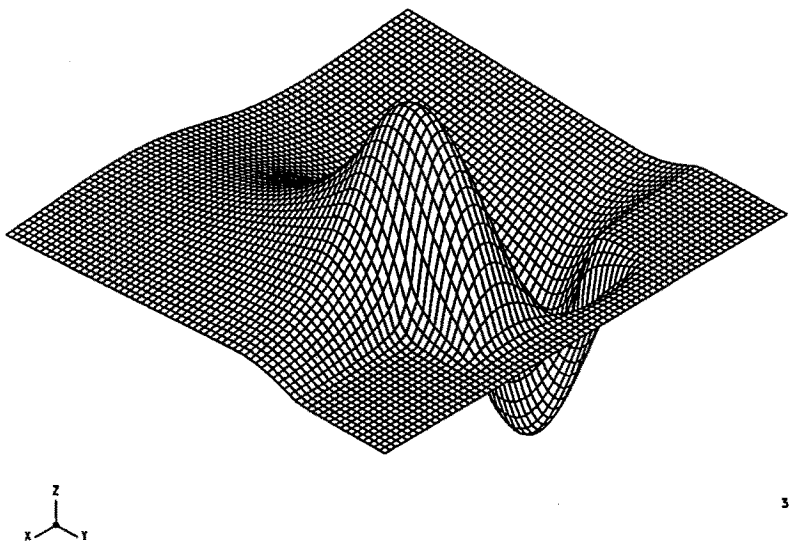


Figure 8B. Leading antisymmetric quasi-TE field profile within the structure UCL1 of reference [36] and Table 6, when $D = H = 0.5\mu\text{m}$ and $\lambda = 1.15\mu\text{m}$.

n_G	n_S	n_C	W μm	$H+D$ μm	X_S μm	Y_S μm	Y_C μm	h_x μm	h_y μm
3.44	3.40	1.0	3	1	2.9901	2.505	0.305	0.01987	0.01

Table 9. The $\text{CaAs}/\text{Ga}_{0.9}\text{Al}_{0.1}\text{As}$ rib waveguide structure UCL1 from Refs. [7–9,14,36,57,58]. (See Figs. 1 and 3 for notation.) The wavelength considered was $\lambda = 1.15\mu\text{m}$. (©IEE [14] 1991)

D :		Quasi-TE		:	Quasi-TM	
μm :	n_{eff}	:	b	:	n_{eff}	b
0.0	3.41196	:	0.2977	:	3.41060	0.2639
0.1	3.41206	:	0.3003	:	3.41069	0.2661
0.2	3.41222	:	0.3042	:	3.41082	0.2693
0.3	3.41243	:	0.3095	:	3.41100	0.2738
0.4	3.41272	:	0.3167	:	3.41124	0.2798
0.5	3.41308	:	0.3257	:	3.41156	0.2877
0.6	3.41353	:	0.3368	:	3.41195	0.2975
0.7	3.41406	:	0.3503	:	3.41244	0.3096
0.8	3.41472	:	0.3665	:	3.41304	0.3246
0.9	3.41554	:	0.3872	:	3.41382	0.3442
1.0	3.41716	:	0.4275	:	3.41546	0.3851

Table 10. Fundamental symmetric modes for the structure UCL1 of Refs. [7–9, 14,36,57,58] and Table 9. ($\lambda = 1.15\mu\text{m}$.) The outer box boundary condition was iteratively corrected exponential decay of field profiles. (©IEE [14] 1991)

D :		Quasi-TE		:	Quasi-TM	
μm :	n_{eff}	:	b	:	n_{eff}	b
0.36:	3.40015	:	0.00383	:		
0.4	3.40068	:	0.01695	:		
0.43:		:		:	3.40017	0.0041
0.45:	3.40146	:	0.0364	:	3.40042	0.0105
0.5	3.40235	:	0.0584	:	3.40116	0.0287
0.6	3.40443	:	0.1102	:	3.40294	0.0732
0.7	3.40694	:	0.1727	:	3.40519	0.1290
0.75:	3.40833	:	0.2073	:	3.40649	0.1613

Table 11. Leading antisymmetric modes for the structure UCL1 of Refs. [7–9, 14,36,57,58] and Table 9. ($\lambda = 1.15\mu\text{m}$.) The outer box boundary condition was iteratively corrected exponential decay of field profiles. (These modes are cut-off by the outer slab modes when $D > 0.75\mu\text{m}$.)

The $D = 1\mu\text{m}$ ($H = 0$) values of n_{eff} and b from Table 10 may be compared with those computed via the usual transcendental equations for a 3-region dielectric slab waveguide [16,19–22] which yield

$$n_{\text{eff}} = 3.41715 \quad \text{and} \quad b = 0.4273$$

for the TE polarization, and

$$n_{\text{eff}} = 3.41546 \quad \text{and} \quad b = 0.3851$$

for the TM mode. Clearly, there is excellent agreement between the transcendental equation and revised SVFD results.

The final single rib waveguide considered here is the COST-216 structure [10] which possesses a buried guiding layer, as shown in Figure 9. Its rib height was chosen to be large enough ($2\mu\text{m}$) so as not to influence the results. Table 12 contains values of the normalized index b for the fundamental symmetric quasi-TE and quasi-TM modes at free-space wavelengths of $\lambda = 1.15\mu\text{m}$ and $1.55\mu\text{m}$; it can be seen that the longer wavelength results lie within the range of values quoted in references [10,67] (which did not consider propagation at the shorter wavelength).

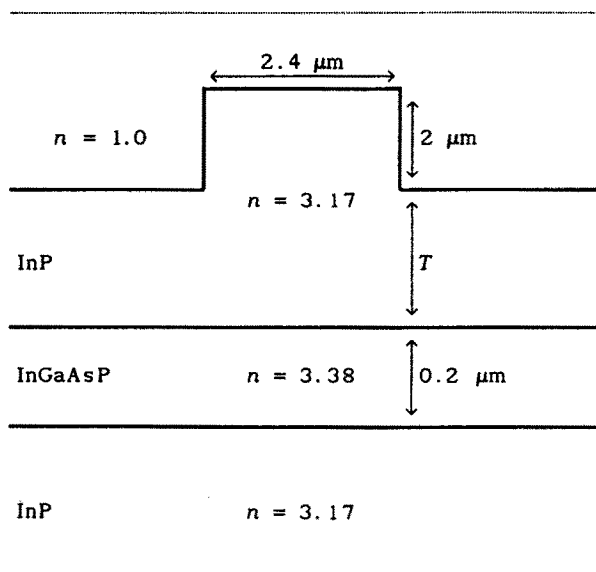


Figure 9. The COST-216 rib waveguide structure of reference [10] where $T = 0.0, 0.2$ and $0.4\mu\text{m}$. (©IEE [14] 1991)

T μm	$\lambda = 1.15 \mu\text{m}$	$\lambda = 1.55 \mu\text{m}$
	Quasi-TE : Quasi-TM	Quasi-TE : Quasi-TM
0.0	0.2416 : 0.2050	0.1181 : 0.0911
0.2	0.2547 : 0.2146	0.1354 : 0.1030
0.4	0.2651 : 0.2252	0.1511 : 0.1170

Table 12. Normalized index b for the fundamental symmetric polarised modes of the rib waveguide structure of Fig. 9 and Refs. [10,14]. The outer box boundary condition was iteratively corrected exponential decay of field profiles. (©IEE [14] 1991)

14. Numerical Results for Rib Waveguide Directional Couplers

The matrix eigenvalue and Rayleigh quotient methods have been employed to directly compute the semi-vectorial propagation supermodes of the COST-216 symmetric rib waveguide directional coupler structure [10] displayed in Figure 10; the rib height was again chosen to be sufficiently large ($2\mu\text{m}$) so as not to influence the results. Table 13 contains polarised values of the coupling length

$$L_C = \lambda/2(n_{eff,e} - n_{eff,o}) \quad (114)$$

in which $n_{eff,e}$ and $n_{eff,o}$ are the modal indices of the fundamental even/symmetric and leading odd/antisymmetric coupler supermodes, respectively, for a given polarization. It is again observed that the longer wavelength ($\lambda = 1.55\mu\text{m}$) results lie within the range of values presented in [10,26,67–69] (where propagation at $\lambda = 1.15\mu\text{m}$ was not considered).

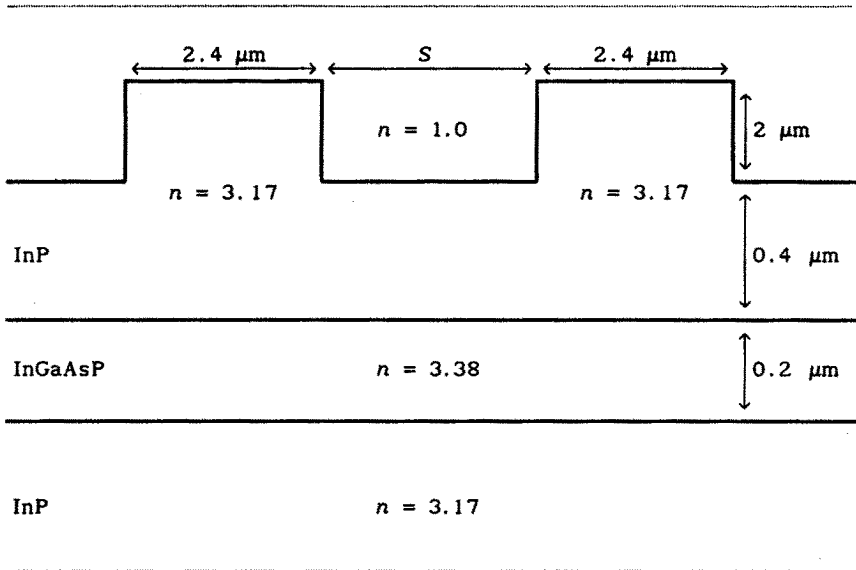


Figure 10. The COST-216 directional coupler structure of reference [10] where $S = 0, 1, 2, 3$ and $4 \mu\text{m}$. (©IEE [14] 1991)

S μm	$\lambda = 1.15 \mu\text{m}$	$\lambda = 1.55 \mu\text{m}$
	Quasi-TE : Quasi-TM	Quasi-TE : Quasi-TM
0	0.219 : 0.182	0.130 : 0.113
1	0.412 : 0.437	0.337 : 0.381
2	0.686 : 0.913	0.669 : 0.958
3	1.115 : 1.881	1.307 : 2.385
4	1.776 : 3.862	2.527 : 5.898

Table 13. Polarised coupling lengths L_c (mm) for the directional coupler structure of Fig. 10 and Refs. [10,14]. The outer box boundary condition was iteratively corrected exponential decay of field profiles. (©IEE [14] 1991)

Contour and surface plots of the fundamental symmetric and leading antisymmetric quasi-TE field profiles at $\lambda = 1.55\mu\text{m}$ are shown in Figures 11(A,B) and 12(A,B), respectively, when the rib separation is $S = 2\mu\text{m}$, whilst plots of the corresponding quasi-TM field profiles are presented in Figures 13(A,B) and 14(A,B). It is observed that there is a greater vertical spread (as expected) of the TM contours when compared with their TE counterparts. The discontinuities in the quasi-TE field amplitude component E_x across the vertical sidewalls of the coupler ribs can just be seen in Figures 11A and 12A, whereas the discontinuities in the quasi-TM component E_y across the horizontal dielectric interfaces are clearly visible in Figures 13A and 14A. Contour plots (not shown) of the polarised \vec{E} -field profiles at $\lambda = 1.15\mu\text{m}$, corresponding to those displayed in Figures 11A-14A and for the same rib separation, experience smaller vertical spreads (as expected because they are further away from cut-off) than their longer wavelength counterparts, with discontinuities again appearing across appropriate dielectric boundaries

15. Numerical Results for Embedded Waveguides

The final structure considered in this chapter is an embedded waveguide [8] whose optical and geometrical parameters are listed in Table 14. Similar structures were studied in reference [70]. Application of the SVFD methods developed in earlier sections has yielded a set of identical values of n_{eff} and b for both E_x and H_y modes, with a corresponding set of identical values for both E_y and H_x modes, over a range of wavelengths. The results are presented, as a function of the free-space wavelength λ , in Table 15. Contour and surface plots of the fundamental E_x and H_y field profiles, at $\lambda = 8.3\text{ mm}$, are displayed in Figures 15(A,B) and 16(A,B), respectively; the discontinuity in E_x across vertical interfaces is clearly visible. Corresponding plots of the fundamental E_y and H_x fields, at $\lambda = 7.5\text{ mm}$, appear in Figures 17(A,B) and 18(A,B), respectively; the discontinuity in E_y across horizontal interfaces can be clearly observed.

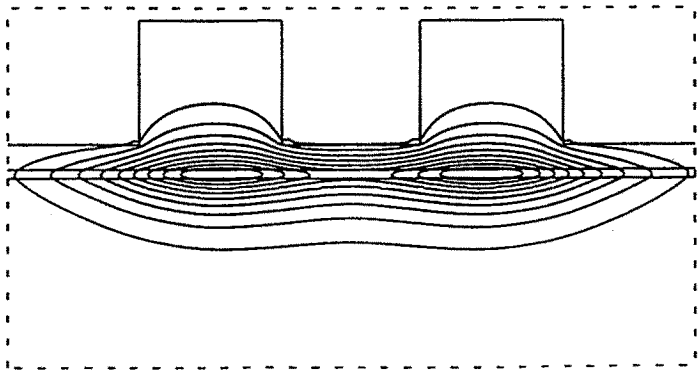


Figure 11A. Fundamental symmetric quasi-TE field profile at $\lambda = 1.55 \mu\text{m}$ for the coupler structure of Figure 10 with $S = 2 \mu\text{m}$. Contour levels are at 10% intervals of the maximum field amplitude. Note the slight discontinuity in E_x across vertical dielectric interfaces. (©IEE [14] 1991)

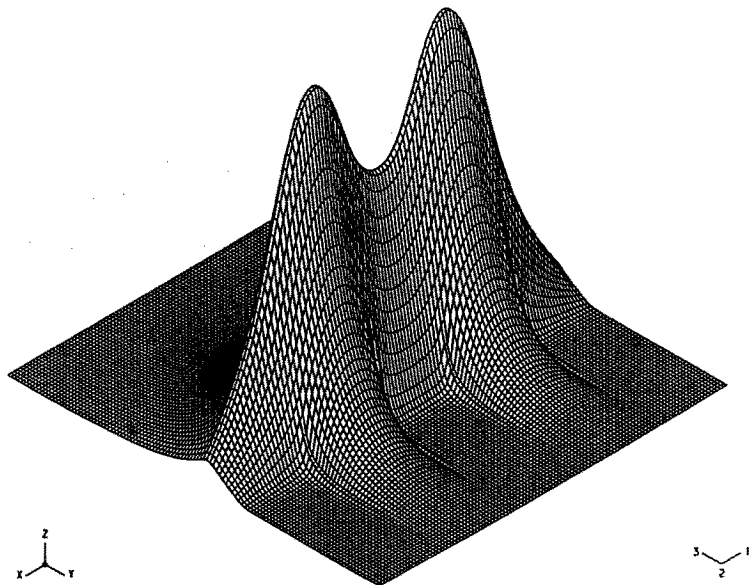


Figure 11B. Fundamental symmetric quasi-TE field profile at $\lambda = 1.55 \mu\text{m}$ for the coupler structure of Figure 10 with $S = 2 \mu\text{m}$.

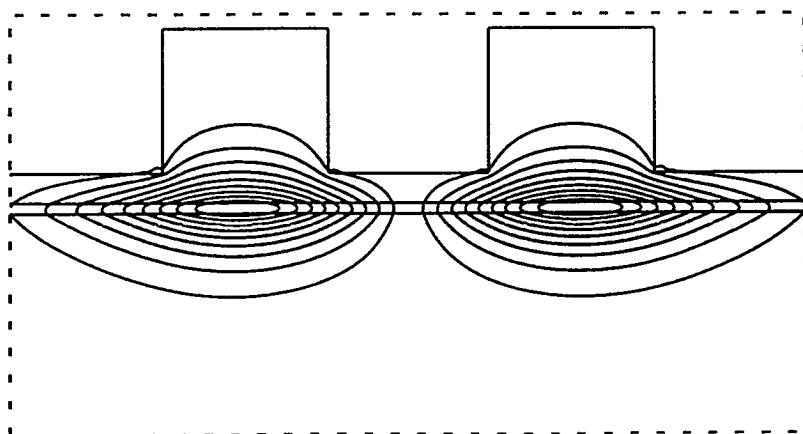


Figure 12A. Leading antisymmetric quasi-TE field profile at $\lambda = 1.55\mu\text{m}$ for the coupler structure of Figure 10 with $S = 2\mu\text{m}$. Contour levels are at 10% intervals of the maximum field amplitude. Note the slight discontinuity in E_x across vertical dielectric interfaces. (©IEE [14] 1991)

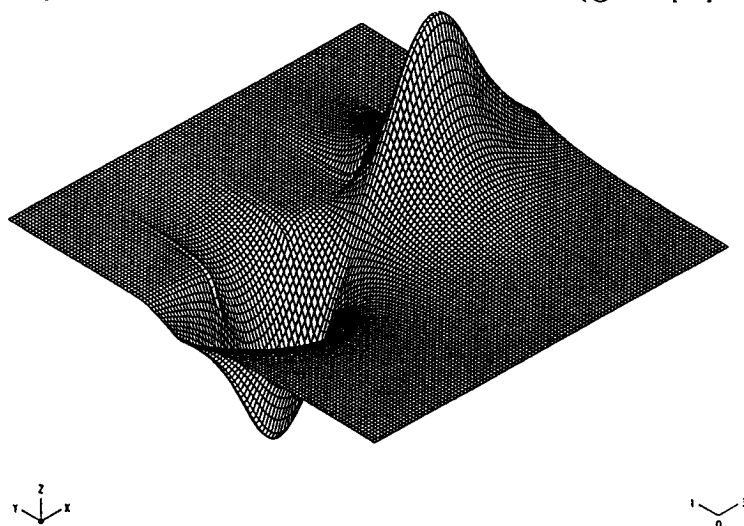


Figure 12B. Leading antisymmetric quasi-TE field profile at $\lambda = 1.55\mu\text{m}$ for the coupler structure of Figure 10 with $S = 2\mu\text{m}$.

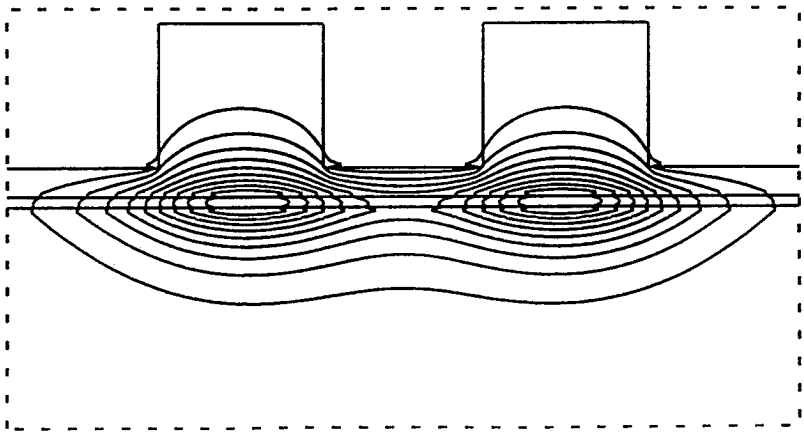


Figure 13A. Fundamental symmetric quasi-TM field profile at $\lambda = 1.55\mu\text{m}$ for the coupler structure of Figure 10 with $S = 2\mu\text{m}$. Contour levels are at 10% intervals of the maximum field amplitude. Note the discontinuity in E_y across horizontal dielectric interfaces. (©IEE [14] 1991)

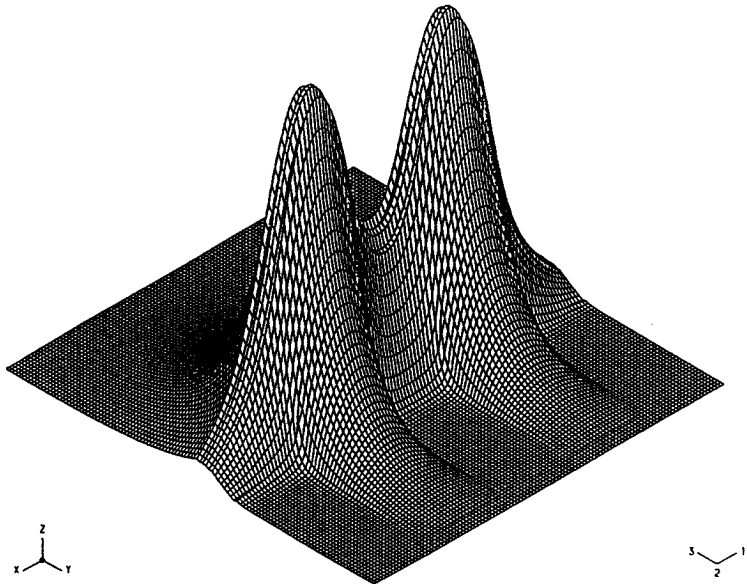


Figure 13B. Fundamental symmetric quasi-TM field profile at $\lambda = 1.55\mu\text{m}$ for the coupler structure of Figure 10 with $S = 2\mu\text{m}$.

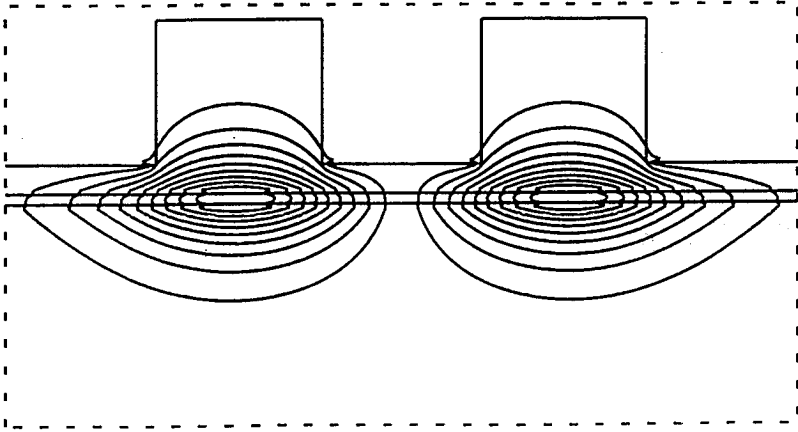


Figure 14A. Leading antisymmetric quasi-TM field profile at $\lambda = 1.55\mu\text{m}$ for the coupler structure of Figure 10 with $S = 2\mu\text{m}$. Contour levels are at 10% intervals of the maximum field amplitude. Note the discontinuity in E_y across horizontal dielectric interfaces. (©IEE [14] 1991)

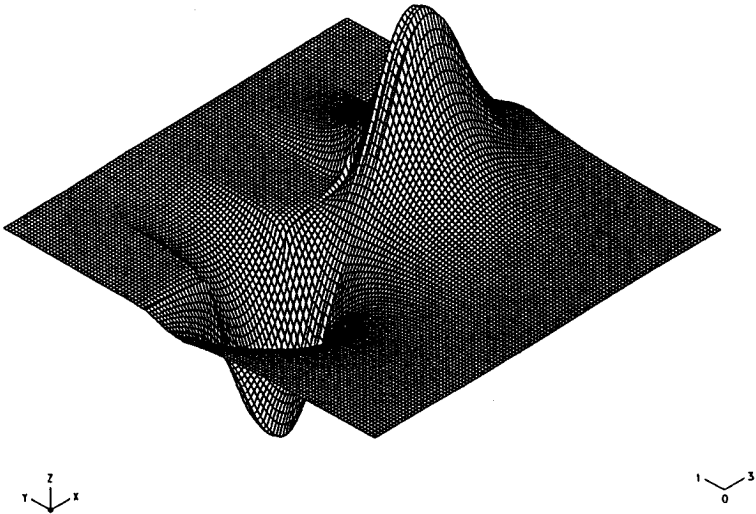


Figure 14B. Leading antisymmetric quasi-TM field profile at $\lambda = 1.55\mu\text{m}$ for the coupler structure of Figure 10 with $S = 2\mu\text{m}$.

n_G	:	n_S	:	n_C	:	W	:	H	:	D	:	X_S	:	Y_S	:	Y_C	:	h_x	:	h_y
:		:		:		mm	:	mm	:	mm	:	mm	:	mm	:	mm	:	mm	:	mm
2.02	:	1.42	:	1.0	:	4	:	1	:	1	:	4.342	:	4.55	:	1.55	:	0.0976	:	0.1

Table 14. An embedded waveguide structure, in the notation of Figs. 2 and 3. (©IEE [8] 1988)

λ	E_x and H_y				E_y and H_x			
	mm	n_{eff}	:	b	:	n_{eff}	:	b
7.50	:	1.567289	:	0.213176	:	1.464701	:	0.062476
7.70	:	1.553501	:	0.192328	:	1.453646	:	0.046844
7.85	:	1.543444	:	0.177239	:	1.446300	:	0.036523
8.00	:	1.533654	:	0.162643	:	1.439876	:	0.027540
8.15	:	1.524151	:	0.148564	:	1.434049	:	0.019426
8.30	:	1.514956	:	0.135024	:	1.429534	:	0.013163

Table 15. Fundamental symmetric E-field and H-field modes, as a function of wavelength, for the embedded waveguide structure of Table 14. The outer box boundary condition was iteratively corrected exponential decay of field profiles. (©IEE [8] 1988)

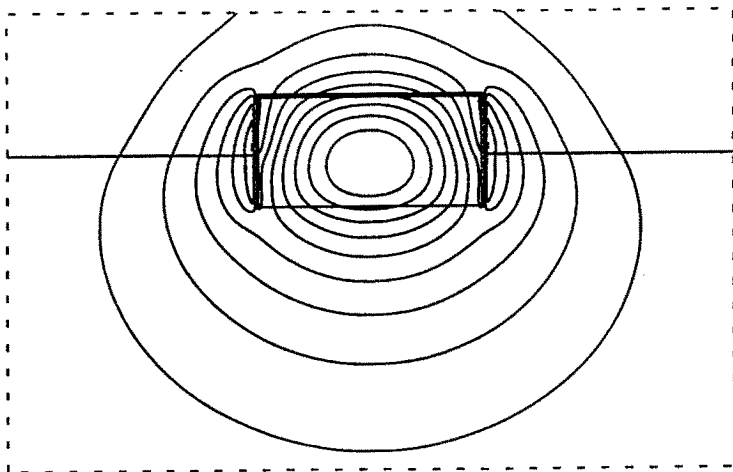


Figure 15A. Fundamental symmetric E_x field profile within the embedded waveguide structure of reference [8] and Table 14, when $\lambda = 8.3$ mm. Contour levels are at 10% intervals of the maximum field amplitude. The discontinuity in E_x across vertical dielectric interfaces is clearly visible.

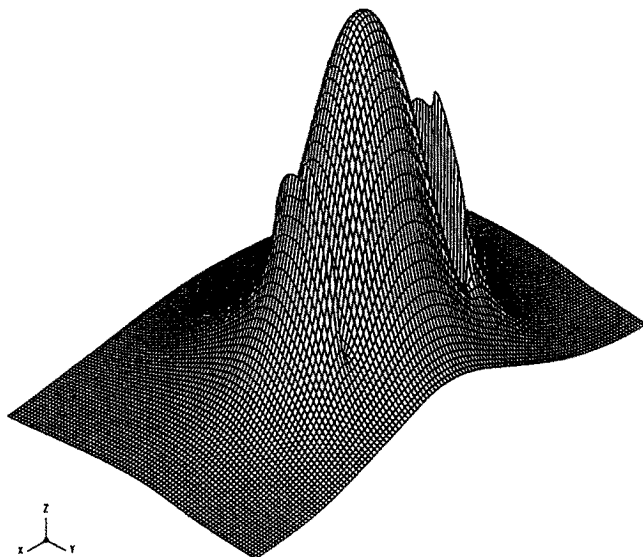


Figure 15B. Fundamental symmetric E_x field profile within the embedded waveguide structure of reference [8] and Table 14, when $\lambda = 8.3$ mm. The discontinuity in E_x across vertical dielectric interfaces is clearly visible.

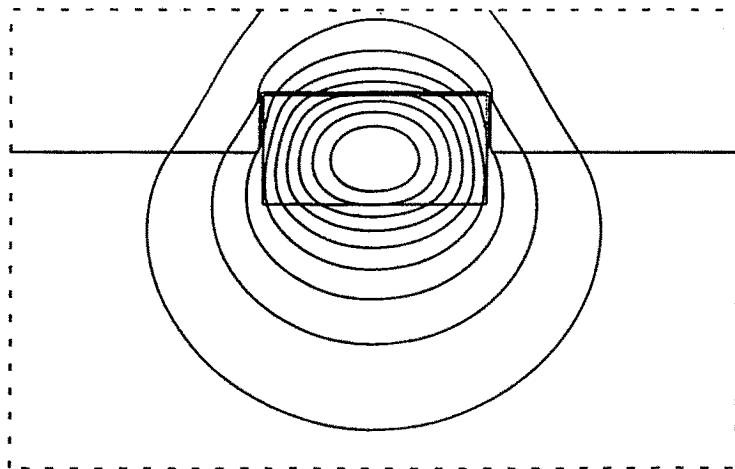


Figure 16A. Fundamental symmetric H_y field profile within the embedded waveguide structure of reference [8] and Table 14, when $\lambda = 8.3$ mm. Contour levels are at 10% intervals of the maximum field amplitude.

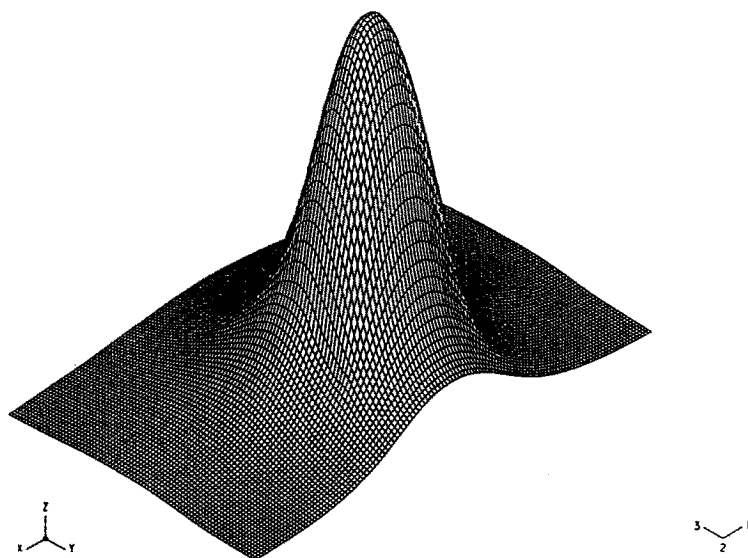


Figure 16B. Fundamental symmetric H_y field profile within the embedded waveguide structure of reference [8] and Table 14, when $\lambda = 8.3$ mm.

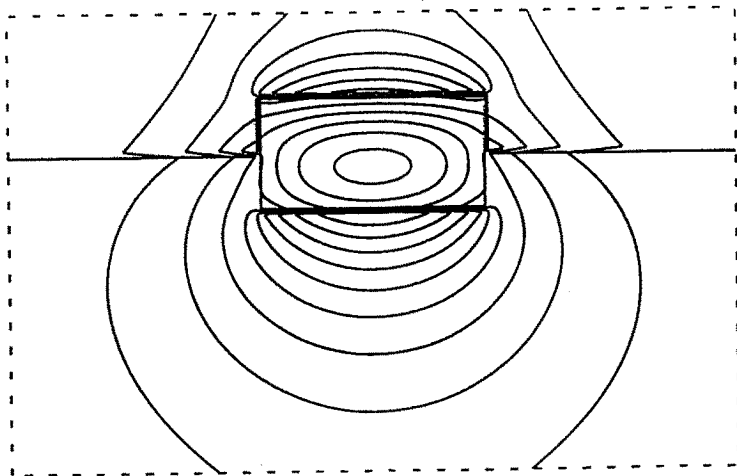


Figure 17A. Fundamental symmetric E_y field profile within the embedded waveguide structure of reference [8] and Table 14, when $\lambda = 7.5$ mm. Contour levels are at 10% intervals of the maximum field amplitude. The discontinuity in E_y across horizontal dielectric interfaces is clearly visible.

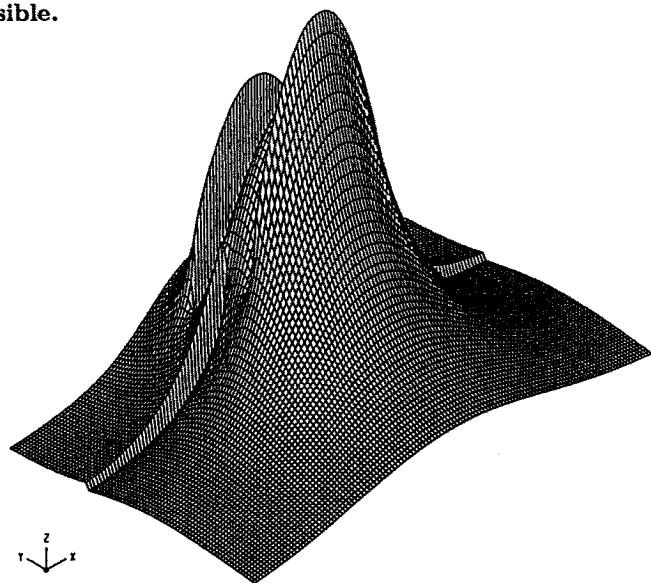


Figure 17B. Fundamental symmetric E_y field profile within the embedded waveguide structure of reference [8] and Table 14, when $\lambda = 7.5$ mm. The discontinuity in E_y across horizontal dielectric interfaces is clearly visible.

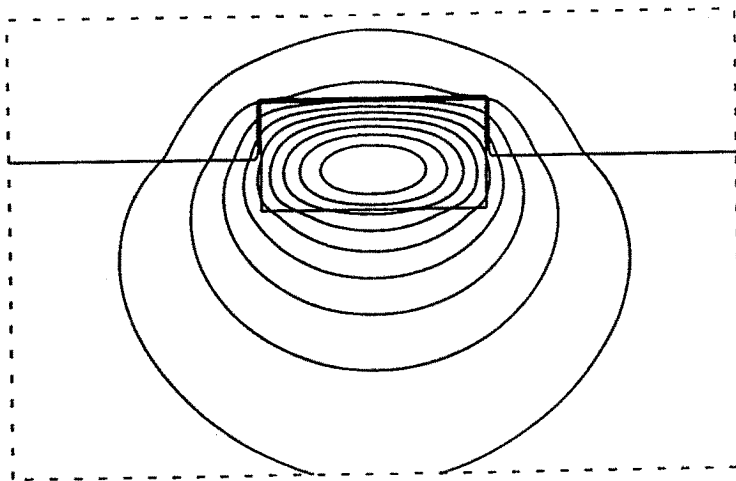


Figure 18A. Fundamental symmetric H_x field profile within the embedded waveguide structure of reference [8] and Table 14, when $\lambda = 7.5$ mm. Contour levels are at 10% intervals of the maximum field amplitude.

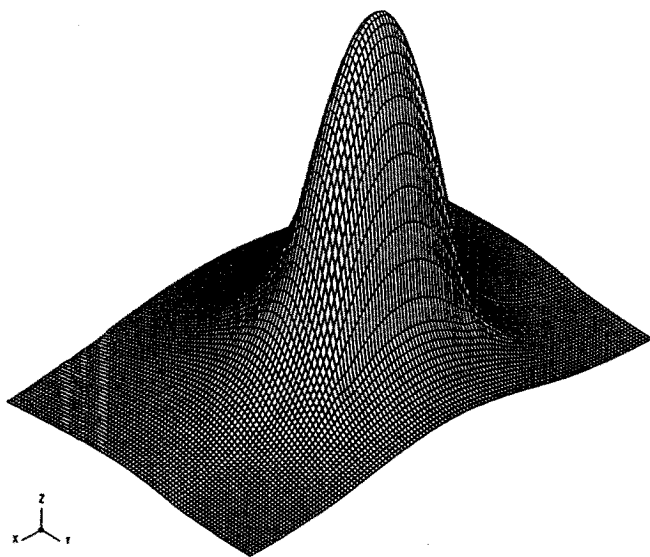


Figure 18B. Fundamental symmetric H_x field profile within the embedded waveguide structure of reference [8] and Table 14, when $\lambda = 7.5$ mm.

16. Conclusion

This chapter has concentrated on finite difference solutions of scalar and semi-vectorial optical waveguiding problems, particularly the latter. Spurious solutions do not arise because the semi-vectorial \overline{E} -field modes of Sections 4 and 5 satisfy the constraint $\nabla \cdot \overline{E} = 0$ via equations (28a) and (45a), respectively, in regions of piecewise constant refractive index, whilst the semi-vectorial \overline{H} -field modes of Sections 6 and 7 observe the $\nabla \cdot \overline{H} = 0$ constraint via equations (53a) and (66a) respectively. The finite difference approximations of the Helmholtz equations for these polarised modes automatically satisfy appropriate continuity and discontinuity conditions at each internal dielectric boundary, with the longitudinally invariant waveguide's transverse refractive index profile having been represented by the rectangular cell array structure illustrated in Figure 3. After any of the four polarised SVFD schemes from Sections 4–7 has been applied at each internal grid point within either the right-hand (or left-hand) half of a waveguide structure which possesses left-right symmetry (as in Figures 1, 2, 9 and 10) or the complete structure when there is no such symmetry (as in asymmetric couplers), the required modal index (111) and corresponding field profile are then determined by either solving the matrix eigenvalue problem (74) or employing the Rayleigh quotient (99) coupled with the SOR equation (101).

Where comparisons are available, it has been found that SVFD yields results which compare very favorably with those produced by full vectorial treatments, as mentioned in sections 13 and 14 and in references [7–9,14,49,64,66]. Moreover, the SVFD approach is conceptually simpler and is more economical in its computer memory and CPU time requirements than are full vector finite element and vector finite difference methods.

SVFD has been validated indirectly: computed values of modal propagation constants and corresponding field profiles have been used in curvature loss calculations [60–62,70]; the resulting theoretical loss values were found to be in excellent agreement with those measured experimentally [60,70]. Thus SVFD can be regarded as a powerful modeling and design tool for planar optical waveguides which contain arbitrary distributions of mutually parallel and orthogonal dielectric discontinuities.

References

1. Benson, T. M., *Integrated optical components produced in GaAs and InP epitaxial layers using the photo-elastic effect*, Ph.D. Thesis, Dept. of Electronic and Electrical Engineering, University of Sheffield, UK, 1982.
2. Schweig, E., and W. B. Bridges, "Computer analysis of dielectric waveguides – a finite difference method," *IEEE Trans.*, MTT-32, 531–541, 1984.
3. Robertson, M. J., S. Ritchie, and P. Dayan, "Semiconductor waveguides: analysis of optical propagation in single rib structures and directional couplers," *IEE Proc. J*, 132, 336–342, 1985.
4. Lagu, R. K., and R. V. Ramaswamy, "A variational finite difference method for analysing channel waveguides with arbitrary index profiles," *IEEE J. Quantum Electron.*, QE-22, 968–976, 1986.
5. Schulz, N., K. Bierwirth, and F. Arndt, "Finite difference analysis of integrated optical waveguides without spurious mode solutions," *Electron. Lett.*, 22, 963–965, 1986.
6. Bierwirth, K., N. Schulz, and F. Arndt, "Finite difference analysis of rectangular dielectric waveguide structures," *IEEE Trans.*, MTT-34, 1104–1114, 1986.
7. Stern, M. S., "Semivectorial polarised finite difference method for optical waveguides with arbitrary index profiles," *IEE Proc. J*, 135, 56–63, 1988.
8. Stern, M. S., "Semivectorial polarised H -field solutions for dielectric waveguides with arbitrary index profiles," *IEE Proc. J*, 135, 333–338, 1988.
9. Benson, T. M., P. C. Kendall, M. S. Stern, and D. A. Quinney, "New results for rib waveguide propagation constants," *IEE Proc. J*, 136, 97–102, 1989.
10. Working Group I, COST-216, "Comparison of different modeling techniques for longitudinally invariant integrated optical waveguides," *IEE Proc. J*, 136, 273–280, 1989.
11. Kim, C. M., and R. V. Ramaswamy, "Modeling of graded index channel waveguides using non-uniform finite difference method," *IEEE J. Lightwave Technol.*, LT-7, 1581–1589, 1989.
12. Schulz, N., K. Bierwirth, F. Arndt, and U. Koster, "Finite difference method without spurious solutions for the hybrid-mode analysis of diffused channel waveguides," *IEEE Trans.*, MTT-38, 722–729, 1990.

13. Seki, S., T. Yamanaka, and K. Yokoyama, "Two-dimensional analysis of optical waveguides with a non-uniform finite difference method," *IEE Proc. J*, 138, 123-127, 1991.
14. Stern, M. S., "Rayleigh quotient solution of semi-vectorial field problems for optical waveguides with arbitrary index profiles," *IEE Proc. J*, 138, 185-190, 1991.
15. Schulz, N., K. Bierwirth, F. Arndt, and U. Koster, "Rigorous finite difference analysis of coupled channel waveguides with arbitrarily varying index profile," *IEEE J. Lightwave Technol.*, LT-9, 1244-1253, 1991.
16. Vassallo, C., *Optical Waveguide Concepts*, Elsevier, Amsterdam-Oxford-New York-Tokyo, 1991.
17. Vassallo, C., "Improvement of finite difference methods for step-index optical waveguides," *IEE Proc. J*, 139, 137-142, 1992.
18. Matin, M. A., T. M. Benson, P. C. Kendall, and M. S. Stern, "New technique for finite difference analysis of optical waveguide problems," *International J. Numerical Modeling: Electronic Networks, Devices and Fields*, Vol. 7, 25-33, 1994.
19. Adams, M. J., *An Introduction to Optical Waveguides*, John Wiley, Chichester, England, 1981.
20. Owyang, G. H., *Foundations of Optical Waveguides*, Edward Arnold, London, England, 1981.
21. Marcuse, D., *Theory of Dielectric Optical Waveguides*, Academic Press, New York, 1974.
22. Ghatak, A. K., and K. Thyagarajan, *Optical Electronics*, Cambridge University Press, England, 1989.
23. Kendall, P. C., M. J. Adams, S. Ritchie, and M. J. Robertson, "Theory for calculating approximate values of the propagation constants of an optical rib waveguide by weighting the refractive indices," *IEE Proc. A*, 134, 699-702, 1987.
24. Robertson, M. J., P. C. Kendall, S. Ritchie, P. W. A. McIlroy, and M. J. Adams, "The weighted index method: a new technique for analysing planar optical waveguides," *IEEE J. Lightwave Technol.*, LT-7, 2105-2111, 1989.
25. P. C. Kendall, M. J. Robertson, P. W. A. McIlroy, S. Ritchie, and M. J. Adams, "Advances in rib waveguide analysis using the weighted index method or the method of moments," *IEE Proc. J*, 137, 27-29, 1990.

26. Robson, P. N., and P. C. Kendall (Eds.), *Rib Waveguide Theory by the Spectral Index Method*, Research Studies Press (Taunton) and John Wiley (Chichester), England, 1990.
27. Kendall, P. C., P. W. A. McIlroy, and M. S. Stern, "Analysis of semiconductor rib waveguides: spectral index method," *Proc. IEE Colloquium on Integrated Optics*, IEE Digest No. 1989/93, 13/1-13/4, 1989.
28. McIlroy, P. W. A., M. S. Stern, and P. C. Kendall, "Fast and accurate method for calculation of polarised modes in semiconductor rib waveguides," *Electron Lett.*, 25, 1586-1587, 1989.
29. McIlroy, P. W. A., M. S. Stern, and P. C. Kendall, "Spectral index method for polarized modes in semiconductor rib waveguides," *IEEE J. Lightwave Technol.*, LT-8, 113-117, 1990.
30. Stern, M. S., P. C. Kendall, and P. W. A. McIlroy, "Analysis of the spectral index method for vector modes of rib waveguides," *IEE Proc. J*, 137, 21-26, 1990.
31. Kendall, P. C., M. S. Stern, and P. N. Robson, "Discrete spectral index method for rib waveguide analysis," *Optical and Quantum Electron.*, 22, 555-560, 1990.
32. Koshiba, M., K. Hayata, and M. Suzuki, "Finite element formulation in terms of the electric field vector for electromagnetic waveguide problems," *IEEE Trans.*, MTT-33, 900-905, 1985.
33. Rahman, B. M. A., and J. B. Davies, "Finite element analysis of optical and microwave waveguide problems," *IEEE Trans.*, MTT-32, 20-28, 1984.
34. Rahman, B. M. A., and J. B. Davies, "Finite element solution of optical waveguides," *IEEE J. Lightwave Technol.*, LT-2, 682-688, 1984.
35. Rahman, B. M. A., and J. B. Davies, "Penalty function improvement of waveguide solution by finite elements," *IEEE Trans.*, MTT-32, 922-928, 1984.
36. Rahman, B. M. A., and J. B. Davies, "Vector-H finite element solution of GaAs/GaAlAs rib waveguides," *IEE Proc. J*, 132, 349-353, 1985.
37. Koshiba, M., K. Hayata, and M. Suzuki, "Improved finite element formulation in terms of the magnetic field vector for dielectric waveguides," *IEEE Trans.*, MTT-33, 227-233, 1985.
38. Young, T. P., and P. Smith, "Finite element modeling of integrated optical waveguides," *GEC J. Research*, 4, 249-255, 1986.

39. Young, T. P., "Design of integrated optical circuits using finite elements," *IEE Proc. A*, 135, 135-144, 1988.
40. Fernandez, F. A., and Y. Lu, "Variational finite element analysis of dielectric waveguides with no spurious modes," *Electron. Lett.*, 26, 2125-6, 1990.
41. Fernandez, F. A., and Y. Lu, "A variational finite element formulation for dielectric waveguides in terms of transverse magnetic fields," *IEEE Trans. Magnetics*, 27, 3864-3867, 1991.
42. Lu, Y., F. A. Fernandez, S. Zhu, and J. B. Davies, "A new variational finite element analysis of microwave and optical waveguides without spurious solutions," *Proc. IEE International Conf. on Computation in Electromagnetics*, IEE Conf. Publ. No. 350, 160-163, 1991.
43. Courant, R., *Differential and Integral Calculus*, Blackie and Son, London and Glasgow, UK, 97-99, 1959.
44. Lennox, S. C., and M. Chadwick, *Mathematics for Engineers and Applied Scientists*, Heinemann, London, England, 20-22, 1977.
45. Fox, L., *An Introduction to Numerical Linear Algebra*, Clarendon Press, Oxford, England, 1964.
46. Wilkinson, J. H., *The Algebraic Eigenvalue Problem*, Clarendon Press, Oxford, England, 1964.
47. Johnson, L. W., and R. D. Riess, *Numerical Analysis*, Addison-Wesley, Reading, Massachusetts, 1977.
48. Atkinson, L. V., P. J. Harley, and J. D. Hudson, *Numerical Methods with FORTRAN-77*, Addison-Wesley, Wokingham (England) and Reading (MA), 1989.
49. Benson, T. M., P. C. Kendall, M. A. Matin, and M. S. Stern, "Polarization correction applied to scalar analysis of semiconductor rib waveguides," *IEE Proc. J*, 139, 39-41, 1992.
50. Fox, L., (Ed.) *Numerical Solution of Ordinary and Partial Differential Equations*, Pergamon Press, Oxford, England, 1962.
51. Smith, G. D., *Numerical Solution of Partial Differential Equations*, Oxford University Press, England, 1965, 1978, 1985.
52. Quinney, D. A., *An Introduction to the Numerical Solution of Differential Equations*, Research Studies Press (Taunton) and John Wiley (Chichester), England, 1985.
53. Huang, W. P., and H. A. Haus, "A simple variational approach to optical rib waveguides," *IEEE J. Lightwave Technol.*, LT-9, 56-61, 1991.

54. Koshiba, M., H. Saitoh, M. Eguchi, and K. Hirayama, "Simple scalar finite element approach to optical rib waveguides," *IEE Proc. J*, 139, 166–171, 1992.
55. Liu, P. L., and B. J. Li, "Semi-vectorial beam propagation method for analyzing polarised modes of rib waveguides," *IEEE J. Quantum Electron.*, QE-28, 778–782, 1992.
56. Liu, P. L., and B. J. Li, "Semi-vectorial Helmholtz beam propagation by Lanczos reduction," *IEEE J. Quantum Electron.*, QE-29, 2385–2389, 1993.
57. Austin, M. W., "Theoretical and experimental investigation of GaAs/GaAlAs and nn GaAs rib waveguides," *IEEE J. Lightwave Technol.*, LT-2, 688–694, 1984.
58. Austin, M. W., "GaAs/GaAlAs curved rib waveguides," *IEEE J. Quantum Electron.*, QE-18, 795–800, 1982.
59. Huang, W. P., and H. A. Haus, "Simple variational approach to optical rib waveguides," *IEEE/OSA Topical Meeting on Integrated Photonics Research*, Hilton Head USA, Tech. Digest Series Vol. 5, 85–86, 1990.
60. Kendall, P. C., M. S. Stern, and P. N. Robson, "A Huygens-type formula for curvature loss from dielectric waveguides in optoelectronics," *Electron. Lett.*, 23, 850–851, 1987.
61. Stern, M. S., P. C. Kendall, and P. N. Robson, "Estimation of rib waveguide radiation losses," *Electron. Lett.*, 24, 17–19, 1988.
62. Kendall, P. C., M. S. Stern, and P. N. Robson, "A new curvature loss formula of Huygens-type for rib waveguides," *IEE Proc. J*, 135, 11–16, 1988.
63. Stern, M. S., P. C. Kendall, R. C. Hewson-Browne, P. N. Robson, and D. A. Quinney, "Scattering loss from rough sidewalls in semiconductor rib waveguides," *Electron. Lett.*, 25, 1231–1232, 1989.
64. Stern, M. S., "Comparison of spectral index, semi-vectorial finite difference and vector finite element methods for the modal analysis of semiconductor optical rib waveguides," *Proc. IEE International Conf. on Computation in Electromagnetics*, IEE Conf. Publ. No. 350, 18–21, 1991.
65. Benson, T. M., P. C. Kendall, and M. A. Matin, "Simple variational approach to optical rib waveguide analysis," *Electron. Lett.*, 28, 1897–1898, 1992.

66. Benson, T. M., P. C. Kendall, M. A. Matin, and M. S. Stern, "Polarised modes of semiconductor rib waveguides," *Electron. Lett.*, 27, 1488-1489, 1991.
67. Mao, Z., and W. P. Huang, "Analysis of optical rib waveguides and couplers with buried guiding layer," *IEEE J. Quantum Electron.*, QE-28, 176-183, 1992.
68. Burke, S. V., "Spectral index method applied to coupled rib waveguides," *Electron. Lett.*, 25, 605-606, 1989.
69. Burke, S. V., "Spectral index method applied to rib and strip-loaded directional couplers," *IEE Proc. J*, 137, 7-10, 1990.
70. Benson, T. M., P. C. Kendall, and M. S. Stern, "Microwave simulation of optoelectronic bending loss in the presence of a dielectric discontinuity," *IEE Proc. J*, 135, 325-331, 1988.